AGU PUBLICATIONS

JGR

Journal of Geophysical Research: Oceans

RESEARCH ARTICLE

10.1002/2014JC009990

Key Points:
- Characterization of global oceanic large-scale baroclinic instabilities
- Comparison of wave-like baroclinic disturbances and planetary Rossby waves
- Identification of decadal modes of variability in the subtropical oceans

Supporting Information:
- Readme
- Supporting figures S1–S9

Correspondence to:
T. J. O'Kane,
terence.okane@csiro.au

Citation:
O'Kane, T. J., R. J. Matear, M. A. Chamberlain, E. C. J. Oliver, and N. J. Holbrook (2014), Storm tracks in the Southern Hemisphere subtropical oceans, *J. Geophys. Res. Oceans*, *119*, 6078–6100, doi:10.1002/2014JC009990.

Received 26 MAR 2014
Accepted 19 AUG 2014
Accepted article online 23 AUG 2014
Published online 16 SEP 2014

Storm tracks in the Southern Hemisphere subtropical oceans

T. J. O'Kane[1,2], R. J. Matear[1,2], M. A. Chamberlain[1,2], E. C. J. Oliver[3,4], and N. J. Holbrook[3,4]

[1]CSIRO Oceans and Atmosphere, Hobart, Tasmania, Australia, [2]Centre for Australian Climate and Weather Research, Hobart, Tasmania, Australia, [3]Institute for Marine and Antarctic Studies, University of Tasmania, Hobart, Tasmania, Australia, [4]ARC Centre of Excellence for Climate System Science, Hobart, Tasmania, Australia

Abstract Ocean storm tracks have previously been associated with the midlatitude western boundary currents (WBCs) and the Antarctic Circumpolar Current (ACC). Here we identify and examine large-scale baroclinically unstable waves occurring within waveguides associated with potential density gradients in the subtropical regions of the Southern Hemisphere (SH) oceans where the trade winds and westerlies meet and at depths associated with mode water formation. In contrast to the Northern Hemisphere subtropics, the SH pathways are more extensive allowing large-scale coherent disturbances to communicate information westward from the midlatitudes to the subtropics (South Pacific Ocean) and from the subtropics to the tropics (Indian Ocean). Particular consideration is given to the subtropical South Pacific Ocean as this is a region where resonant interactions between large-scale Rossby waves and significant topographic features have been reported to occur. Using an ocean general circulation model and a simple potential energy transfer diagnostic, we identify the relevant nonlinearly modified structures comparing their propagation characteristics to planetary Rossby waves calculated using a shallow water model. Although at first appearance baroclinic disturbances resemble planetary Rossby waves, we show they are inherently nonlinear, multiscale and are amplified where topography occurs. The location of the disturbances coincides with regions of high variability in sea surface height observed in satellite altimetry and their speeds closely match the large-scale coherent westward propagating structures described in the observational literature. Our study provides evidence that, in addition to the midlatitude WBCs and the ACC, significant ocean storm tracks are also manifest in the SH subtropics.

1. Introduction

The ocean primarily responds to large-scale O(1000) km, low-frequency O(1)year changes in atmospheric forcing through the generation of long wavelength baroclinic Rossby waves [*Gill*, 1982]. These planetary Rossby waves travel westward with typically slow speeds $O(10^{-1})$–$O(10^{-2})$ m s^{-1} and long wavelengths of $O(10^{6})$–$O(10^{5})$ m through the subtropics to midlatitudes. They are only weakly expressed in sea surface height (SSH) $O(10^{-1})$m, but are nevertheless readily detected using satellite altimetry [*Chelton and Schlax*, 1996; *Wang et al*., 1998; *Fu and Chelton*, 2001; *Challenor et al*., 2004; *Maharaj et al*., 2007, 2009]. Rossby wave propagation is often identified using Hovmoller phase diagrams of SSH anomalies [*Chelton and Schlax*, 1996] or depth of an isotherm [*Kessler*, 1990].

Rossby waves are known to display complex interactions with bottom topography [*Chelton and Schlax*, 1996; *Killworth and Blundell*, 1999; *Tailleux*, 2003]. This is particularly true where they impinge on steep isolated structures, resulting in the anomalously slow phase speeds observed in satellite observations of SSH [*Maharaj et al*., 2005] in the South Pacific. More recently, higher-resolution satellite altimetric observations suggest that these features can, on shorter time scales, be regarded as persistent nonlinear quasi-stable mesoscale eddies rather than linear planetary Rossby waves [*Chelton et al*., 2011]. This has prompted renewed investigations into the nature of Rossby waves and eddies [*Early et al*., 2011].

Here we are motivated to understand the dynamics by investigating the stability of the flow and the disturbances, often multiscale, that give rise to long lived or metastable coherent structures. Whereas *Williams et al*. [2007] examined and contrasted the role of eddy vorticity in the respective atmosphere and midlatitude ocean ($>35^{\circ}$ latitude) storm tracks, it has generally been less well recognized that waveguides also occur in the subtropical regions of the Southern Hemisphere (SH). Here our focus is on the subtropics and

in particular, the structure of large-scale nonlinearly modified baroclinic oceanic Rossby waves. We show that the subtropical SH waveguides are much more extensive in comparison to those in the Northern Hemisphere (NH), indeed the South Indian and South Pacific Ocean pathways have no NH equivalent. These pathways allow for greater communication between the SH midlatitude-subtropical-tropical regions through westward propagating baroclinic disturbances.

We focus particular attention on the South Pacific where studies of Rossby wave propagation have primarily attempted to reconcile discrepancies between propagation speeds observed by altimetry and the expected planetary Rossby wave speeds taken from corrections to linear theory [*Maharaj et al*., 2007, 2009]. We propose that it is in fact large-scale (nonlinear) baroclinic Rossby waves that are the dynamical mechanism determining the observed surface height variability in the subtropical band and offer a general framework to explain them.

In particular, we are interested in addressing the following points:

1. To characterize baroclinic pathways (waveguides) in the SH using an OGCM of comparable resolution to current climate models and compare to observational (subsurface) products.

2. To investigate whether such pathways provide plausible teleconnections within/between the respective midlatitude-subtropical-tropical regions of the SH oceans.

3. To examine if the propagation characteristics and multiscale nature of large baroclinic disturbances along these pathways are realistic—in particular, in the South Pacific where significant topographic interactions are known to occur and linear theories break down.

Because of the complexity of oceanic Rossby waves, previous studies have largely relied on linear theories and often in a quasi-geostrophic setting. Given the substantive literature of linear instability analysis (reviewed in section 2), we instead characterize baroclinic disturbances without recourse to linear theory. To this end we employ a simple mean to transient potential energy diagnostic [*Orlanski and Cox*, 1973; *Gill et al*., 1974; *Oey*, 2008]. Our approach is to use an OGCM forced by atmospheric reanalysis data. We first compare pathways in the subtropical regions of the SH oceans characterized by significant horizontal density gradients with those in the NH. We further compare Eady growth periods of the modeled pathways to observational estimates calculated from Argo data. We use anomaly root mean square (RMS) error and complex Hilbert empirical orthogonal functions [*Hannachi et al*., 2007] to characterize the propagation of low-frequency baroclinic disturbances in each of the SH oceans before focusing on the South Pacific Ocean pathway, which encapsulates the complexity of the problem. We describe the excitation and propagation of baroclinic disturbances confined within a density gradient "waveguide" connecting the ACC in Drake's Passage across the subtropical South Pacific Ocean into the East Australian Current (EAC) and via the East Auckland Current to enter the ACC at the East Pacific Rise. We further detail the propagation of these disturbances in the subtropical South Pacific Ocean using 2-D Radon transform analysis, which are contrasted with estimates of westward propagating linear first baroclinic-mode Rossby waves simulated in an ocean (reduced gravity) shallow water model (SWM). We also examine the stability of this teleconnection and formulate an instability-driven dynamical perspective of the formation and propagation of the observed low-frequency baroclinic wave-like structures that are analogous to the theory of storm tracks in the atmosphere. In the next section 2, we briefly review the literature. In section 3, we describe the OGCM and the 1 1/2 layer SWM used to calculate linear Rossby wave propagation. Sections 4, 5, and 6 contain the results, discussion, and conclusions respectively.

2. Background

Tailleux [2005] examined the energy paths of long extratropical oceanic Rossby waves. He found a weak dependence on the zonal wave number ratio τ where the zonal phase speed varies approximately linearly with the meridional wave number. In such cases, he shows that the propagation becomes quasi nondispersive and describable at leading order in terms of topography and stratification alone. Using raypaths, *Tailleux* [2005] found three regimes. The first is associated with a topographic regime following the constant f/hc (where c is a constant determined by the strength of the stratification, f the Coriolis parameter, and h the ocean depth). The second and third correspond to fast and slow westward regimes, largely independent of topography and associated with the first and second bottom-pressure-compensated normal modes

[*Tailleux and McWilliams*, 2001, 2002]. *Chen and Kamenkovich* [2013] examined the role of bottom topography in the linear baroclinic instability of zonal flows on a β-plane and compared to the effects of both zonal and meridional topographic slope. Through varying the lower-level background potential vorticity gradient, they found that zonal slopes always act to destabilize background zonal flows.

Since the pioneering works of *Charney* [1947], *Eady* [1949], *Phillips* [1954], *Smagorinsky* [1963], *Pedlosky* [1964], and *Green* [1974], it is well known that baroclinically unstable waves may develop in regions of the atmosphere where horizontal temperature gradients are large. Such baroclinic disturbances are ubiquitous across a wide range of scales. Like atmospheric fronts, the ocean displays large-scale fronts with characteristic slopes determined by density gradients, differential rotation, and the vertical shear of the currents parallel to the front. *Orlanski and Cox* [1973] examined baroclinically unstable waves in an idealized Gulf Stream simulation. They demonstrated that the formation of large-scale meanders of the jet is associated with disturbance growth rates smaller than those predicted by linear theory. This implies nonlinear effects are of primary importance. Using a regional ocean forecasting system, *Oey* [2008] extended this approach to characterize regions of flow instability responsible for deep eddy formation in the Gulf of Mexico.

Gill et al. [1974] studied the partition of energy in the main oceanic gyres, and in particular, the Sargasso Sea. Assuming quasigeostrophy, *Gill et al*. [1974] showed that the potential energy in the gyres is 1000 times greater than the kinetic energy. Initiated by the action of the mean wind field, the production of mid-ocean eddies is known to occur via conversion of the potential energy of the mean flow into transient energy (subsequently referred to as eddies). By relating the mean velocity profile to the average slope of the isopycnals $f^2\bar{U}_z/N^2\beta = \frac{f}{\beta}\frac{\bar{\rho}_y}{\bar{\rho}_z}$ (where $\bar{U}$ is the component of the current in the x direction, $\bar{\rho}$ the mean density, f the Coriolis parameter, β the differential rotation and N^2 the buoyancy frequency), it has been determined that the manner in which the horizontal density gradient varies with depth is the major factor affecting mean to transient potential energy conversion and stability.

Gill et al. [1974] further considered small (linear) perturbations to the mean state and found that the propagation velocities and vertical structure of the longer baroclinically unstable waves (eddies with wavelengths of 300–500 km) were close to those of first baroclinic-mode (planetary) Rossby waves. Considering the change of phase with depth of disturbance velocity profiles, they identified that energy transfer takes place in the upper 400 m for the subtropical gyres. *Halliwell et al*. [1994] examined the role of nonlinearity in the Sargasso Sea subtropical frontal zone. They focused on the transfer of energy to longer wavelengths once the wave number spectrum has saturated. Their work emphasized equal roles for baroclinic energy conversion and atmospheric forcing in generating eddy variability in the subtropical frontal zones. This approach is analogous to examinations of the relationship of baroclinicity in the zonal winds to latitudinal gradients of mean temperature through the thermal wind balance $\frac{\partial u_g}{\partial z} = -\frac{R}{fH}\frac{\partial T}{\partial y}$ in the atmosphere. Here H is the scale height, R the gas constant, and $\frac{\partial u_g}{\partial z}$ relates the vertical geostrophic wind shear to the horizontal temperature gradient $\frac{\partial T}{\partial y}$.

Using a wind forced $2\frac{1}{2}$ layer model, *Cerovecki and de Szoeke* [2007] found that the intensification of long period waves in the southwestern region of ocean basins could arise due to the spatial growth of purely time periodic, but baroclinically unstable, motions. *Smith* [2007] presented a systematic analysis of linear instability characteristics of the oceanic mean state comparing the most energetic growing modes to observations of eddy statistics. *Tulloch et al*. [2009] examined altimetric phase speeds via adjustment of the lateral scale of linear Rossby wave theory to best fit altimetric observations of westward phase propagation. They found that in order to fit linear theory to altimetric observations one must assume that a transition from waves to turbulence occurs at $\sim\pm 30^\circ$ of latitude. *Tulloch et al*. [2009] conducted a local linear stability analysis of the hydrographic Ocean Comprehensible Atlas (OCCA), a 3 year climatology for 2004–2006 on a $1^\circ \times 1^\circ$ horizontal grid, to ascertain the growth rates and scales of the fastest growing modes. Again using predictions from linear theory, they found that the fastest growing modes in the subtropics and gyre interiors have a scale varying between 0.5 and 1 times the Rossby radius of deformation and e-folding scale of several weeks. Importantly, they find little evidence for an extended inverse energy cascade throughout the oceans, especially in the eddy-rich regions driven by larger-than deformation-scale baroclinic instabilities. *Williams et al*. [2007] examined baroclinic and barotropic instability over a 10 year period of altimetric data 1992–2002 (Ocean Topography Experiment (TOPEX)/Poseidon and European Remote Sensing Satellite (ERS)) making a direct analogy between enhanced regions of eddy variability in the eddy-rich regions of the midlatitude oceans and atmospheric storm tracks. Presumably, because of the weaker eddy activity and

spatial and temporal resolution of the available observational data, none of these previous studies consider the subtropical regions.

More generally, in order to distinguish the unstable waves from the baroclinic planetary waves, one would ideally like to measure the energy exchange due to long-term (low frequency) correlations between density perturbations and velocity perturbations. Additionally, in order to estimate the rate of energy conversion, we require an estimate of the variation of the mean horizontal density gradient with depth. *O'Kane et al*. [2013] employed this approach to examine the propagation and amplification of low-frequency baroclinically unstable waves in the Antarctic Circumpolar Current (ACC). They found amplification of baroclinically unstable waves occurred in regions characterized by significant density gradients, bottom topography, and Rossby waves, and that these disturbances initiated transitions between quasi-stable thermocline regimes. This result is analogous to that of *Frederiksen* [1982] who showed that baroclinic instability is an important mechanism for enabling the atmosphere to transition between quasi-stationary states associated with atmospheric blocking and a zonal flow. Both of these studies show that for many regimes in geophysical flows, baroclinic instability is often seen to initiate the transition between metastable states whereas barotropic instability determines the life time of the particular state.

3. Models

3.1. Model Configuration

Our primary model is the Australian Community Climate Earth System Simulator-Ocean (ACCESS-o) configuration of the U.S. National Oceanic and Atmospheric Administration Geophysical Fluid Dynamics Laboratory (GFDL) version 4p1 of the Modular Ocean Model (MOM4p1) ocean-ice code [*Delworth et al*., 2006]. The model configuration is as described by *O'Kane et al*. [2013] so we make our description here brief. The configuration is volume conserving—Boussinesq using z^* coordinates scaled in the vertical. Weak restoring is applied to the surface salinity of the top layer (equivalent thickness of 10 m) which is relaxed to World Ocean Atlas (WOA09) [*Antonov et al*., 2010; *Locarnini et al*., 2010] fields with a time scale of 60 days to reduce drift. We use the temporal residual mean [*McDougall and McIntosh*, 1996] to parameterize the transport of passive tracers, temperature, and salinity. The K-Profile Parameterization scheme [*Large et al*., 1994] is applied to mixing in the vertical.

We employ the tripolar ACCESS-o model grid [*Uotilla et al*., 2012]. This grid is a 360×300 logically rectangular horizontal mesh, overlying an orthogonal curvilinear grid whereby a singularity at the north pole is avoided by using a tripolar grid following *Murray* [1996]. This approach also provides reasonably fine resolution in the Arctic Ocean while at the same time enhancing computational efficiency. Along the curvilinear zonal direction, ACCESS-o has a regular spaced grid with 1° resolution. In the meridional direction, the grid spacing is nominally 1° resolution, with the following three refinements:

1. Tripolar Arctic north of 65°N.

2. Equatorial refinement to $1/3^\circ$ between 10°S and 10°N.

3. A Mercator (cosine dependent) implementation for the SH, ranging from $1/4^\circ$ at 78°S to 1° at 30°S.

In the vertical direction, ACCESS-o implements the z^* coordinate available in MOM4p1, with 50 model levels covering 0–6000 m with a resolution ranging from 10 m in the upper layers (0–200 m) to about 333 m for the abyssal ocean. Although not eddy resolving, this model resolves large-scale Rossby waves and energy transfers associated with transient disturbances that may become resonant with the resolved Rossby waves.

The model simulations described in this study employ atmospheric fields from the Coordinated Ocean-Ice Reference Experiments (COREs) [*Griffies et al*., 2009] for global ocean-ice modeling. For our experimental configuration, we use the CORE.v2 interannually varying forcing (1948–2007) (hereafter CORE2) [*Large and Yeager*, 2004, 2009]. The CORE2 data sets, support code, and documentation were accessed from the GFDL MOM4 Data Sets website (http://data1.gfdl.noaa.gov/nomads/forms/mom4/COREv1.html and COREv2.html).

3.2. Shallow Water Model

A global 1° resolution $1\frac{1}{2}$–layer linear reduced-gravity SWM as described in *Holbrook et al*. [2011] is used to calculate Rossby wave propagation across the South Pacific Ocean. The model comprises an active upper

layer of uniform density overlying a deep motionless layer of larger uniform density. These density layers are separated by an interface that approximates the ocean pycnocline. The reduced gravity, g', reflects the density difference between the upper and lower layers, where the lower layer is assumed to be motionless and infinitely deep. The SWM takes account of the geographically varying first baroclinic-mode gravity wave speeds, c_1, provided by *Chelton et al.* [1998] to generate geographically varying values for g'. Thus, geographic variations in $g'(x,y)=c_1^2(x,y)/H$, where H is assumed to be a constant depth of 300 m, are more realistic in regions of large density gradients around bathymetric features and in terms of the west-east sloping thermocline and its zonal gradient in stratification. The upper layer is forced by wind stress anomalies from CORE2. The long Rossby waves manifest as westward propagating anomalies in the pycnocline depth. The model formulation permits Ekman pumping and both Rossby and Kelvin wave propagation along the pycnocline to be generated in response to the large-scale wind stress forcing. Note that both ACCESS-o and the shallow water model are forced with the same CORE2 surface winds.

3.3. Diagnostics

3.3.1. Potential Energy Conversion

We very simply describe baroclinic disturbances using mean—transient potential energy transfers. Here we express the energy transfers in terms of time-means (overbar) and fluctuations (prime) [*Mata et al.*, 2006; *Oey*, 2008; *O'Kane et al.*, 2013]:

$$\bar{\Phi}=\frac{\overline{u'\rho'}\frac{\partial\bar{\rho}}{\partial x}+\overline{v'\rho'}\frac{\partial\bar{\rho}}{\partial y}}{\frac{\partial\bar{\rho}}{\partial z}} \tag{1}$$

where ρ is the potential density and $\tilde{\rho}$ is the reference state approximated as the horizontal average of the time mean. u and v are the horizontal velocity components in the x and y (zonal and meridional) directions, respectively. These energy transfer terms are calculated on each level using 60 (CORE2 and component simulations) years of output from the ACCESS-o model. Instantaneous transfers are obtained by removing the time averaging of the transient terms u', v', ρ' and will be denoted as Φ' (10^3 kg m^2 s^{-1}). Here Φ' represents the flux of mean potential energy to transient potential energy through baroclinic disturbances about the mean flow [*Haidvogel and Beckmann*, 1999]. Positive values in equation (1) indicate the conversion of mean to transient potential energy. Transient mechanisms are involved with both the generation and dissipation of potential energy to and from the mean flow. Note that equation (1) has characteristics similar to the Eady growth rate [*Eady*, 1949].

3.3.2. Eady Growth Rate

The reciprocal of the Eady growth rate maximum defines characteristic time scales for eddies to be formed by baroclinic instability. As in *Eady* [1949], *Williams et al.* [2007], and the recent study of *Tulloch et al.* [2009], we define the Eady growth rate maximum to be

$$\omega_{BI}=0.31\left|\frac{f}{N}\frac{\partial U}{\partial z}\right| \tag{2}$$

where f is the Coriolis parameter, N^2 is the buoyancy frequency, and $\frac{\partial U}{\partial z}\sim\Delta U/H$ is the vertical shear in the background flow where H is the depth.

3.3.3. Complex (Hilbert) EOFs

Rasmusson et al. [1981] first introduced the now standard method of complex Hilbert empirical orthogonal functions (EOFs) to identify propagating signals in atmospheric science problems. The procedure we follow is to first take the Hilbert transform of the time series and then construct a complex covariance matrix from the resulting complex time series. Complex Empirical Orthogonal Functions (CEOFs) are then constructed such that for each mode n we have complex eigenvectors $E_n(\mathbf{x})$ and principal components $P_n(t)$ with corresponding spatial and temporal phases $\theta_n(\mathbf{x})$ and $\phi_n(t)$ as well as amplitudes $|E_n|$ and $|P_n|$. Power spectra are calculated via periodograms (Fast Fourier Transform) of the real part of the principal components $\Re(P_n)$. Reconstructed spatial maps of the respective modes are given by $R_n=|E_n|(\cos\theta_n+\sin\theta_n)$.

Merrifield and Guza [1990] note the limitations of using complex Hilbert EOFs where nondispersive waves are present. *Oey* [2008] also suggests caution in their interpretation when applied to deep eddies and instabilities. *Hannachi et al.* [2007] comprehensively review the literature and methodology of using EOFs. Here we recognize that for the regions we are considering quasi-nondispersive waves may be present and there

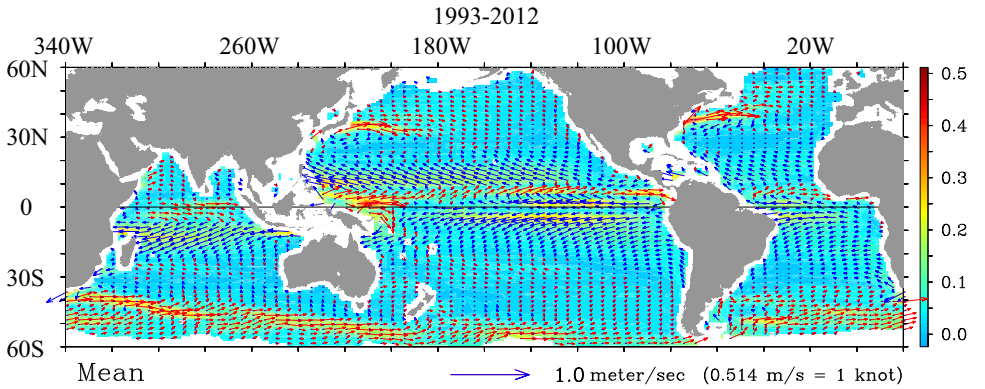

Figure 1. Mean ocean surface currents (m/s) for the period 1993–2012 derived from satellite altimetry and scatterometer data and generated from the NOAA OSCAR website www.oscar.noaa.gov as described in *Bonjean and Lagerloef* [2002].

is the possibility that the variance may be anomalously spread amongst several complex Hilbert EOF (CEOF) propagating modes. While we also calculated the phase velocity, as in *Oey* [2008], via $c_n = \frac{d\phi_n/dt}{\nabla\theta_n}$, we primarily employ CEOFs to understand the spatial structure of the baroclinically unstable modes and to ascertain if they propagate.

3.3.4. The 2-D Radon Transform

Subsequent CEOF analysis of Φ' in the SH subtropics (section 4) showed the existence of many significant modes (multiscale) limiting their ability to succinctly characterize variability. We therefore use Radon transforms, including back projection, to avoid the potential pitfalls of CEOFs, and separate the propagating modes into their characteristic time scales. The Radon transforms supplement the CEOF results and are more readily physically interpretable. To calculate propagation characteristics of Rossby waves, we employ a 2-D Radon transform (2-D-RT) analysis defined by

$$\Re f(t,\theta) = \int_{l_{t,\theta}} f ds = \int_{s=-\infty}^{\infty} f(t\cos\theta - s\sin\theta, t\sin\theta + s\cos\theta) ds \tag{3}$$

where f is a function of Cartesian coordinates x and y and $\Re f$ is a function of polar coordinates [*Freeman*, 2010]. The 2-D-RT is applied to Hovmoller plots of propagating anomalies as a function of longitude which have first been time centered and standardized. The characteristic propagation times are the tangent of the angles at which the local maxima occur and the phase speeds are simply calculated thereafter. We further employ the inverse Radon transform, or back projection, to isolate linear, nonlinear, and quasi-stationary modes from the forward 2-D-RT energy-projection angle peaks.

4. Results

4.1. A Comparison of Waveguides by Hemisphere

The potential energy of the large-scale mean ocean circulation is generated by the action of the large-scale mean wind field. Figure 1 depicts the observed mean climatological surface currents calculated from years (1993–2012) of satellite altimetry and scatterometer data and generated from the NOAA OSCAR website www.oscar.noaa.gov using the method described by *Bonjean and Lagerloef* [2002]. Here we see the largest vectors in the Kuroshio and Gulf Stream boundary current regions, the equatorial regions and the ACC. We also notice the mid-ocean gyres in the subtropics where the interface between the trade winds and westerlies occurs are also clearly visible. These regions coincide with the subtropical oceanic fronts and are coincident with significant horizontal density gradients that are in part determined by the wind stress and also bottom topography. These regions are also evident in altimetry as regions of large variability.

In Figure 2, we show the standard deviation of mean sea level anomalies (MSLA) from AVISO in the SH for all Augusts between 1993 and 2008. We have chosen to show the August MSLA as it is a time of maximum eddy activity and baroclinic instability in the subtropics and in particular the South Pacific Ocean [*Qiu and Chen*, 2004]. The major regions of large variability (areas of blue to purple) are: (Southern) the ACC, (Atlantic) the Brazil-Malvinas confluence, (Pacific) the EAC extending across the Pacific from the South Equatorial

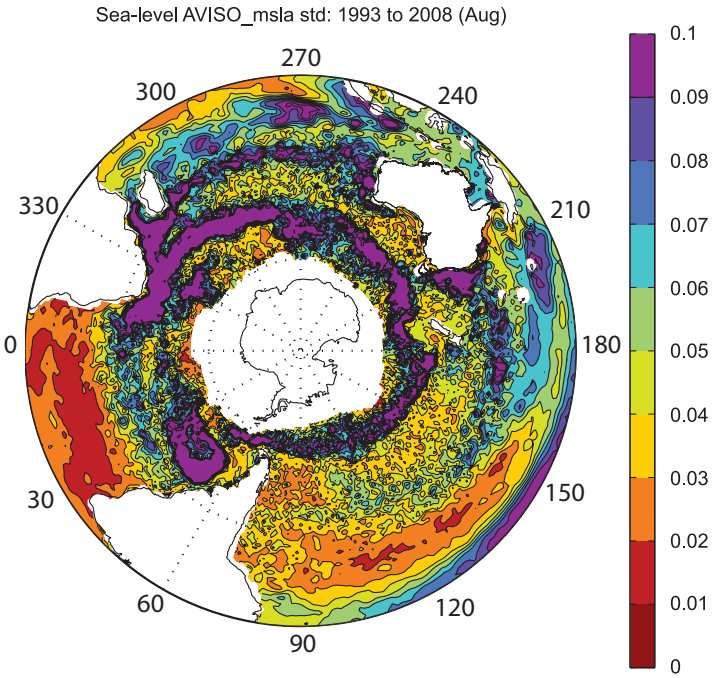

Figure 2. Standard deviation (m) of mean sea level anomalies from AVISO satellite altimetry for all Augusts between 1993 and 2008. Longitudes are in °W.

Current, and (Indian) from the Western Australian coast to Madagascar. For the subtropics, large-scale low-frequency wave-like disturbances occur as the result of unstable baroclinic processes in the subtropical mode water (STMW) region between about 150 and 350 m depth [*Halliwell et al*., 1994; *Holbrook and Maharaj*, 2008]. STMW forms during wintertime mixed layer convective deepening and produces a lens of mode water, that separates from the surface mixed layer, extending through the subsurface between about 150 and 300 m depth, at least in the southwest Pacific [*Holbrook and Maharaj*, 2008]. Therefore, there is a strong seasonality in the persistent eddies [*Halliwell et al*., 1994]. The large-scale wind forcing determines the structure of the horizontal density gradients as well as providing the source of potential energy for generating eddies. The AVISO MSLA standard deviation indicates regions of observed large eddy variability. Comparison of Figures 1 and 2 shows these regions are also coincident with large horizontal potential density gradients, indicative of frontal regions and where significant interaction with topography occurs, e.g., the region 30°S between 190°W and 150°W in the South Pacific. Eddy activity in the Indian Ocean South Equatorial Current is also largest in winter due to the large-scale wind variability [*Tchernia*, 1980].

A comparison of our model mean potential density contours (averaged over 150 to 350 m depth) to the mean surface currents from OSCAR (Figure 1) shows regions of significant horizontal density gradients in the model are consistent with observations (Figure 3a). The RMS of the buoyancy frequency (N^2) provides a map of significant vertical density variations and, when depths between 150 and 350 m are considered, is an indicator of the statically unstable regions of the tropical to subtropical oceans (Figure 3b) that are characteristic of mode waters [*Talley*, 1999; *Holbrook and Maharaj*, 2008]. For example, the tropical instability waves of the equatorial Pacific are particularly associated with large values of N^2. Outside of the tropics significant values of N^2 are to be found in the subtropical frontal regions. For example, in the southeastern Indian Ocean near the southwestern coast of Australia, we see two branches in the N^2 anomaly RMS. The first and most obvious Indian Ocean branch extends from Western Australia to Madagascar along 30°S consistent with altimetric observations, the second is between 20°S and 30°S. A third but weak pathway runs along the Western Australian coast connecting to the equator. However, this branch is not well resolved by our model and we will not mention it further.

Accounting for the small difference in scale, comparison of the SSH anomalies RMS (Figure 3c) to the AVISO MSLA standard deviation (Figure 2) shows good agreement in both magnitude and extent particularly in the subtropics. In the South Pacific, there is only one path or waveguide extending from the Chilean coast near 40°S to the east Australian coast near 20°S and largely coincides with large-scale Rossby wave propagation along the midlatitude to subtopical South Pacific waveguide [*Wang et al*., 1998; *Maharaj et al*., 2005].

Thermal anomalies (SST) are a direct indicator of thermocline disturbances and identify regions where the coupling to the atmosphere is important (Figure 3d). The major coupling to the atmosphere occurs, as expected, in the tropics in the central and eastern Pacific but also in the Indian Ocean near the coast of Java. Outside of the tropics, the Kuroshio and Gulf Stream regions are noticeable, as are the subtropical frontal regions of the South Pacific and also in the Pacific sector of the ACC.

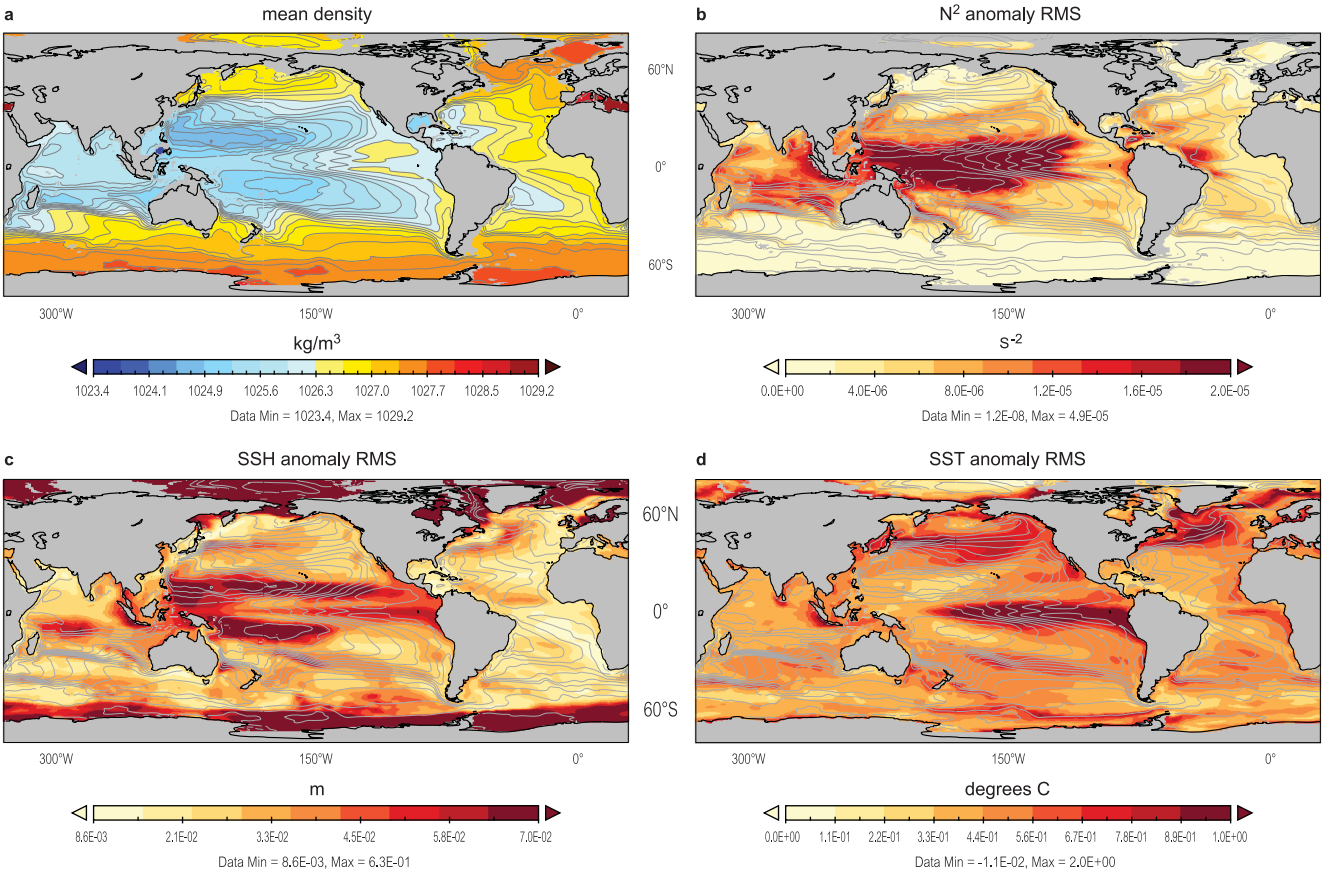

Figure 3. (a) Simulated climatological mean potential density averaged over 150–350 m depth for the period 1948–2007. (b) RMS of anomalous Brunt-Vaisala bouyancy frequency averaged over 150—350 m depth, (c) SSH anomaly RMS and (d) SST anomaly RMS all with simulated climatological mean potential density contours as in Figure 3a overlaid.

A direct calculation of baroclinic instability according to equation (1) (Figure 4a) and taking the RMS (averaged over depths 150–350 m) reveals a much clearer picture of where large-scale coherent wave-like disturbances might be expected to occur. Disregarding the tropical instability waves and focusing on the subtropics, we see baroclinically unstable waves are indeed confined to the waveguides determined by the mean horizontal density gradients and their variation with depth. In particular, the dual pathways from the southwest Western Australian coast to Madagascar and the central Indian Ocean are very clearly defined. Large horizontal density gradients associated with the Agulhas Current in the Indian Ocean extend to the southern tip of Africa and across the Atlantic to South America where they are associated with the confluence of the Brazil-Malvinas currents and the Sub-Antarctic Front. We also note two isolated regions along the Somali coast, again associated with horizontal density gradients. The Bay of Bengal is also strongly represented although baroclinic instability in this region is largely driven by freshwater fluxes from river runoff and saltwater intrusions from the Arabian Sea associated with the monsoon. As expected in the South Pacific, the EAC and Tasman Front connection across to the East Auckland Current manifests as a region where eddy variability is dominated by baroclinic processes. A coherent pathway from the Chilean coast to about 180°W is also evident. Regions of large baroclinic instabilities in the South Pacific are in close agreement with the AVISO MSLA observations shown in Figure 2. These thermocline disturbances travel westward in the subtropics along subtropical gyre pathways that are further associated with the intermediate and surface branches of the global Atlantic meridional overturning circulation as discussed by *Speich et al.* [2007].

In Figure 4b, we show the inverse of the Eady growth rate maximum in the model, again averaged over 150–350 m depth and calculated over the period 1948–2007. The time scales and locations of the waveguides compare well to an observational estimate (supporting information Figure S1) (1°×1° resolution) calculated using monthly T and S fields from the World Ocean Atlas (WOA09) and monthly velocity and

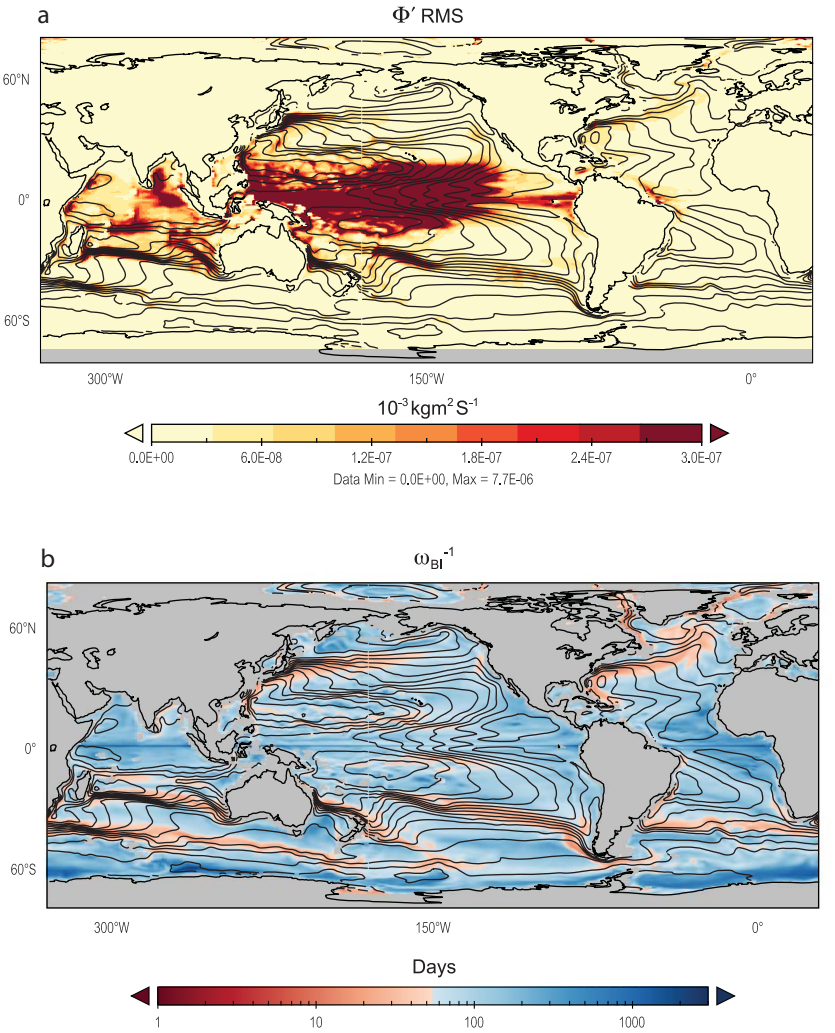

Figure 4. (a) RMS of Φ', and (b) modeled estimate of the inverse of the *Eady* growth rate ω_{BI} averaged over 150—350 m depth for the period 1948–2007 and with climatological mean potential density contours overlaid.

monthly climatalogical density estimates based on Argo data gathered over the period December 2004 to November 2010 as described by *Gray and Riser* [2014]. The pathways in the observational estimate are broader due to the uniform 1° grid and the use of climatalogical fields whereas the ACCESS-o model has regions of refinement in the meridional direction and averages monthly mean values of the Eady growth rate. In both observations and model, the fastest growth is localized within regions of significant horizontal density gradients. The Eady growth period isolates regions where vertical shears are most important and provides a more standard measure of baroclinic instability. Here we see growth periods ranging from 20 to 50 days in the regions of significant potential density gradients associated with the SH subtropical gyre regions and also in the western boundary currents with slightly longer periods for the Antarctic Circumpolar Current greater than ∼50 days. The time scales and spatial patterns of both the modeled and observational growth periods are comparable to those of Figure 4b of *Williams et al*. [2007] based on the observed Levitus climatology on a 1° grid averaged over the upper 250 m. This close agreement between model and observations provides additional confidence in the realism of our model configuration.

The clear presence of strong horizontal and vertical gradients on the pole side of the subtropical gyres which act as waveguides for baroclinic disturbances and that the subtropical SH waveguides or storm tracks are much more extensive in relation to those in the NH are major points are significant findings of this work. This allows the possibility for greater communication between the midlatitudes and the subtropical regions via coherent westward propagating baroclinic disturbances. In particular, the South Indian Ocean

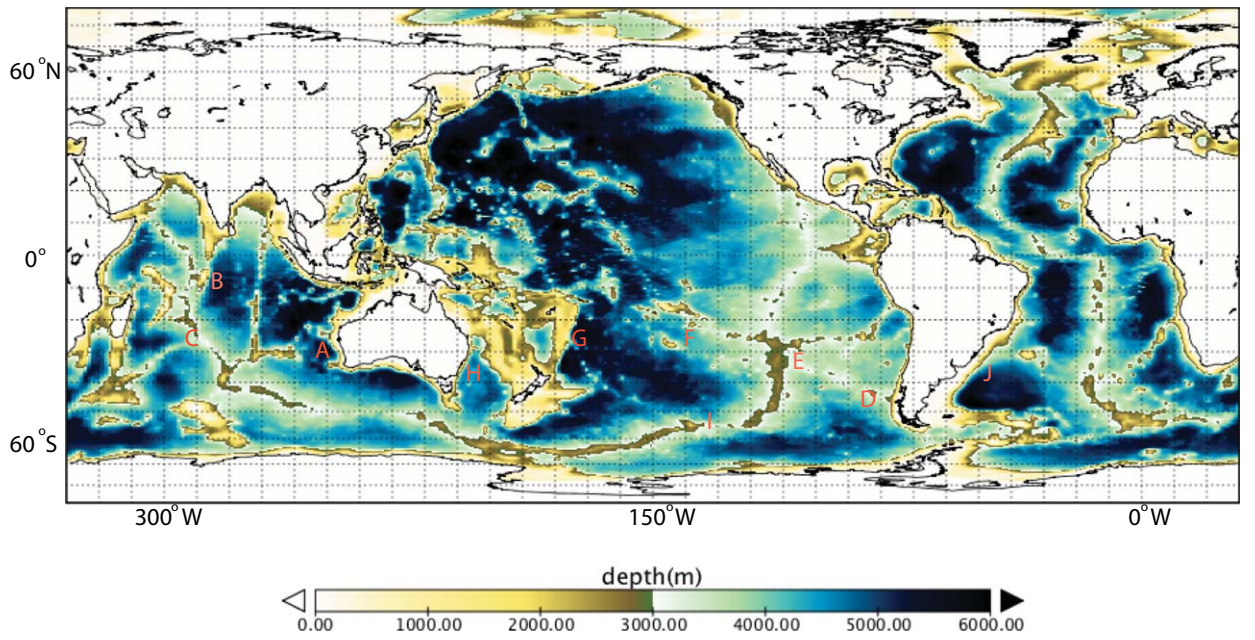

Figure 5. Model topography in meters (m). Grid spacing shown is 10°×10°. Major topographic features of significance are: A, Perth Basin 30°S–250°W; B, Chagos-Laccadives Ridge 5°S–15°S290°W; C, Central Indian Ridge 20°S–30°S290°W; D, Chile Rise 38°S90°W; E, East Pacific Rise 30°S–40°S110°W; F, Cook-Austral seamount chain at 20°S–30°S150°W; G, Kermadec Ridge 20°S–30°S180°W; H, Tasman Sea 30°S–40°S190°W–210°W; I, East Pacific Rise 58°S150°W–130°W; J, Brazil-Malvinas Confluence 40°S50°W.

has two major branches from the western Australian coast to Madagascar, whereas the South Pacific waveguide extends from the coast of Chile to, and as we will show in section 4.2.3, ultimately communicate with the East Australian Current. Importantly the South Indian and South Pacific Ocean pathways have no comparable NH analogue.

4.2. Propagation Characteristics

We now consider each of the following SH subtropical gyre regions where baroclinic instabilities are most evident: the South Indian Ocean, the South Atlantic Ocean near the Brazil-Malvinas Confluence, and the South Pacific. The South Pacific (including the East Australian Current) will be discussed in greater detail in section 4.2.3. We have calculated the leading 20 CEOFs of Φ' and potential temperature averaged over all levels between 100 and 350 m depth but discuss in detail only the leading four here. In all cases to be considered, the leading 20 CEOFs account for more than 95% of the variance but the eigenvalue spectrum is relatively flat. This is indicative of a lack of scale separation and that more than a few of the leading principal components (PCs) are required to explain a significant amount of the variance. Locations of significant topographic interaction with baroclinic disturbances are indicated in Figure 5.

4.2.1. South Indian Ocean

For the Indian Ocean south of 5°S, disturbances (Figure 6) are evident along the pathways described in Figures 3 and 4. The spatial phase, amplitude, and reconstructed modes are shown for the leading four CEOFs. Regions of large amplitude correspond to areas in which disturbances amplify within the waveguide. As the (temporal) phase decreases in time (supporting information Figure S3), here westward propagation corresponds to continuous decrease in (spatial) phase along the regions of large amplitude (Figure 6, left column). Note also that the spatial patterns of the real and imaginary components of the leading four CEOFs (supporting information Figure S2) are in quadrature. Periodograms show power at a range of values between 12 and 120 months with no dominant frequency (supporting information Figure S3). The spectrum of the leading 20 eigenvalues (not shown) is relatively flat indicating that the observed disturbances are the result of the superposition of many modes. This is also reflected in the explained variances of the leading four CEOFs, which together account for only 48.4% of the variance. For the Indian Ocean, baroclinic disturbances are shown to propagate along two distinct pathways; one following the South Equatorial Current from the southwest tip of Western Australia and to the southeast coast of Madagascar. The second runs along the Western Australian coast extending into the central Indian Ocean region located between 15°S–5°S and

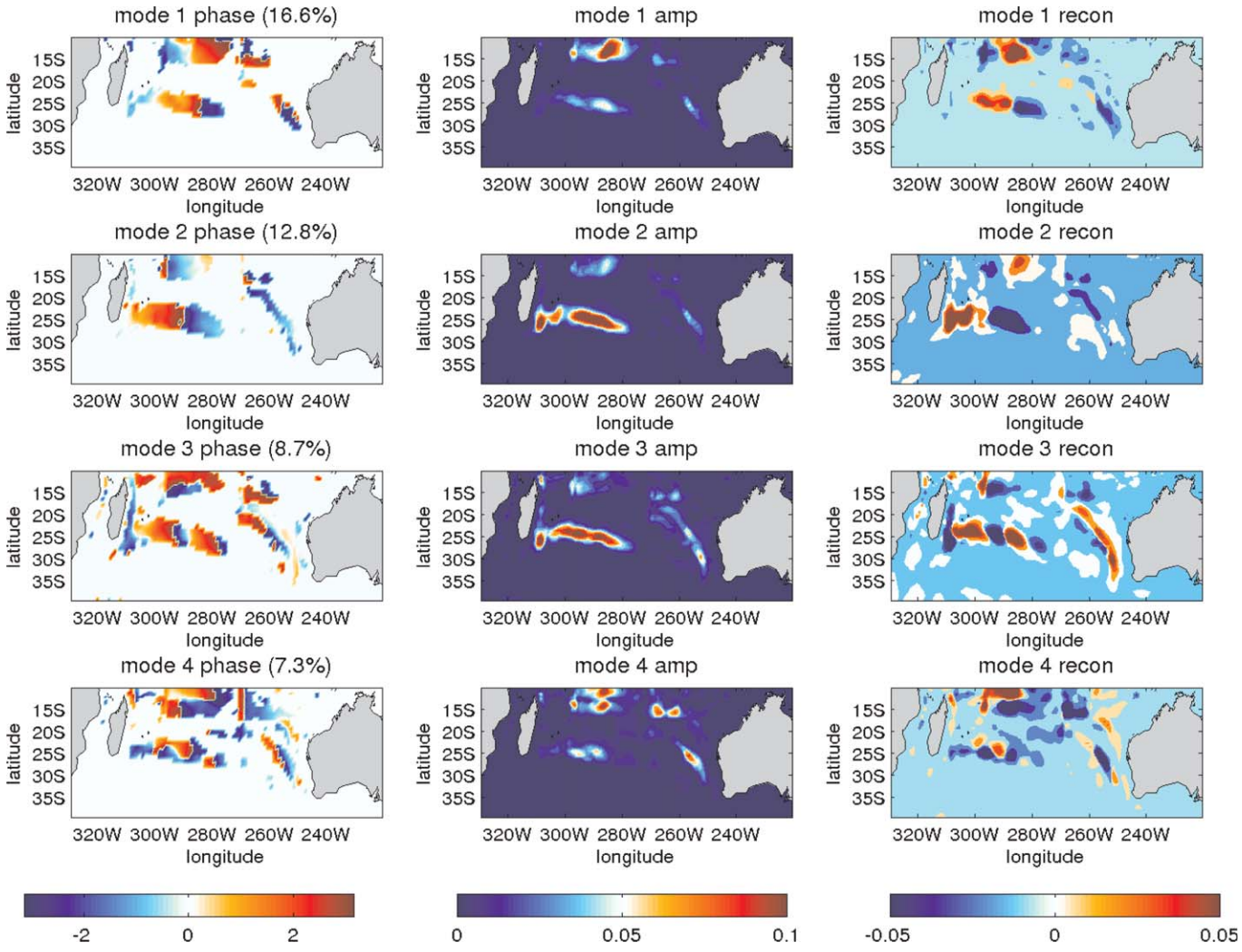

Figure 6. CEOFs of Φ' for the South Indian Ocean. (left column) Spatial patterns of phase, (middle column) amplitude, and (right column) reconstructed mode for the leading four CEOFs with explained variance indicated. The phase is only shown where the amplitude is ≥ 0.01. The corresponding temporal amplitudes, phase and phase portraits are shown in supporting information Figures S2 and S3.

290°W–270°W (also evident in SSH Figure 3c). Between 5°S and 15°S mode 1 displays largest amplitudes are in the vicinity of the Chagos-Laccadives Ridge. For modes 2 and 3 (Figure 6), the largest amplitudes occur where the Southwest Indian Ridge meets the Central Indian Ridge (25°S, 290°W). The reconstructed mode 3 most clearly projects onto the upper waveguide in the region of the Perth basin and extending from 35°S to 20°S.

CEOF analysis of potential temperature (Figure 7) shows mode 3 to be the dominant propagating mode in the region of 270°W–240°W. This mode has a period of $\approx$ 8 years (supporting information Figure S4) and is probably related to low-frequency variability in the latitudinal extent of the dense subtropical mode waters. These large temperature variations are most clearly associated with the generation of disturbances along the upper South Indian Ocean pathway.

4.2.2. South Atlantic Ocean

In the South Atlantic, baroclinic instability is associated with eddy formation in the region of the Brazil-Malvinas confluence and is largely confined to the upper 600 m. The dynamics of this region are generally poorly understood; however, this region is also associated with the formation of a persistent and coherent positive SSH (anticyclonic) anomaly in the vicinity of the Brazil-Malvinas confluence, commonly referred to as the Zapiola Eddy. While baroclinic processes are associated with eddy formation once formed, the

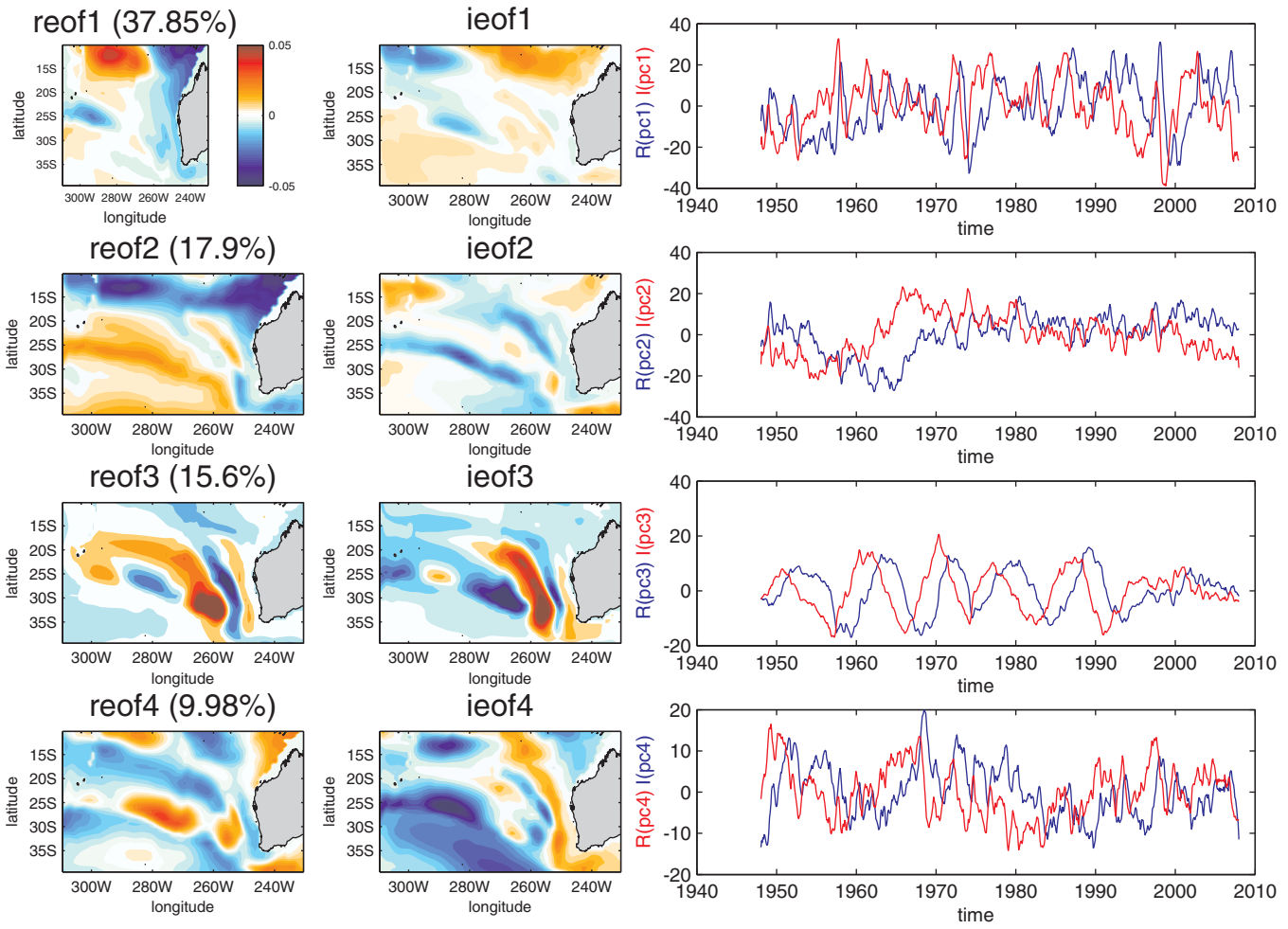

Figure 7. Complex EOFs (CEOFs) of potential temperature anomalies for the South Indian Ocean averaged over 100–350 m depth. Spatial patterns are shown for the (left column) real and (middle column) imaginary parts as well as (right column) the corresponding temporal components (PCs) for the leading four CEOFs. The explained variance for each CEOF is indicated in the left column. The corresponding temporal amplitudes and phase are shown in supporting information Figure S4.

Zapiola Eddy assumes an equivalent barotropic structure such that barotropic instability, often enhanced by additional momentum fluxes due to interaction with topography, largely determines the life time of the eddy [*de Miranda et al.*, 1999; *Volkov and Fu*, 2008]. This mechanism, whereby the potential vorticity of barotropic eddies become anticorrelated with the contours of the topography, was first described by *Bretherton and Haidvogel* [1976] with the subsequent statistical dynamics developed by *O'Kane and Frederiksen* [2004] and *Frederiksen and O'Kane* [2005].

The leading four CEOFs of Φ' in the South Atlantic (Figure 8) are confined within the region of largest horizontal density gradients (Figure 4a) between 35°S and 45°S and extending from 55°W to the east reaching 20°W. The spatial patterns of the real and imaginary parts of the leading four CEOFs (supporting information Figure S5) are in quadrature and have greatest expression in the region of the confluence, and combined explain $\approx$ 62% of the variance. The phase portraits clearly show these to be propagating modes.

The largest mode 1 amplitudes occur in the region 55°W–40°W with periods between 3 and 5 years (supporting information Figure S6). Mode 2, while occupying the same longitudinal extent, has a much longer period (>10 years) whereas mode 3 has signal at 2 and $\approx$ 8 years. For potential temperature (Figure 9), the variance is again largely located within the waveguide regions. Modes 1–3 all show evidence of propagation (quadrature: see also supporting information Figure S6) with the mode 1 periodogram showing no significant periods less than 5 years (supporting information Figure S7).

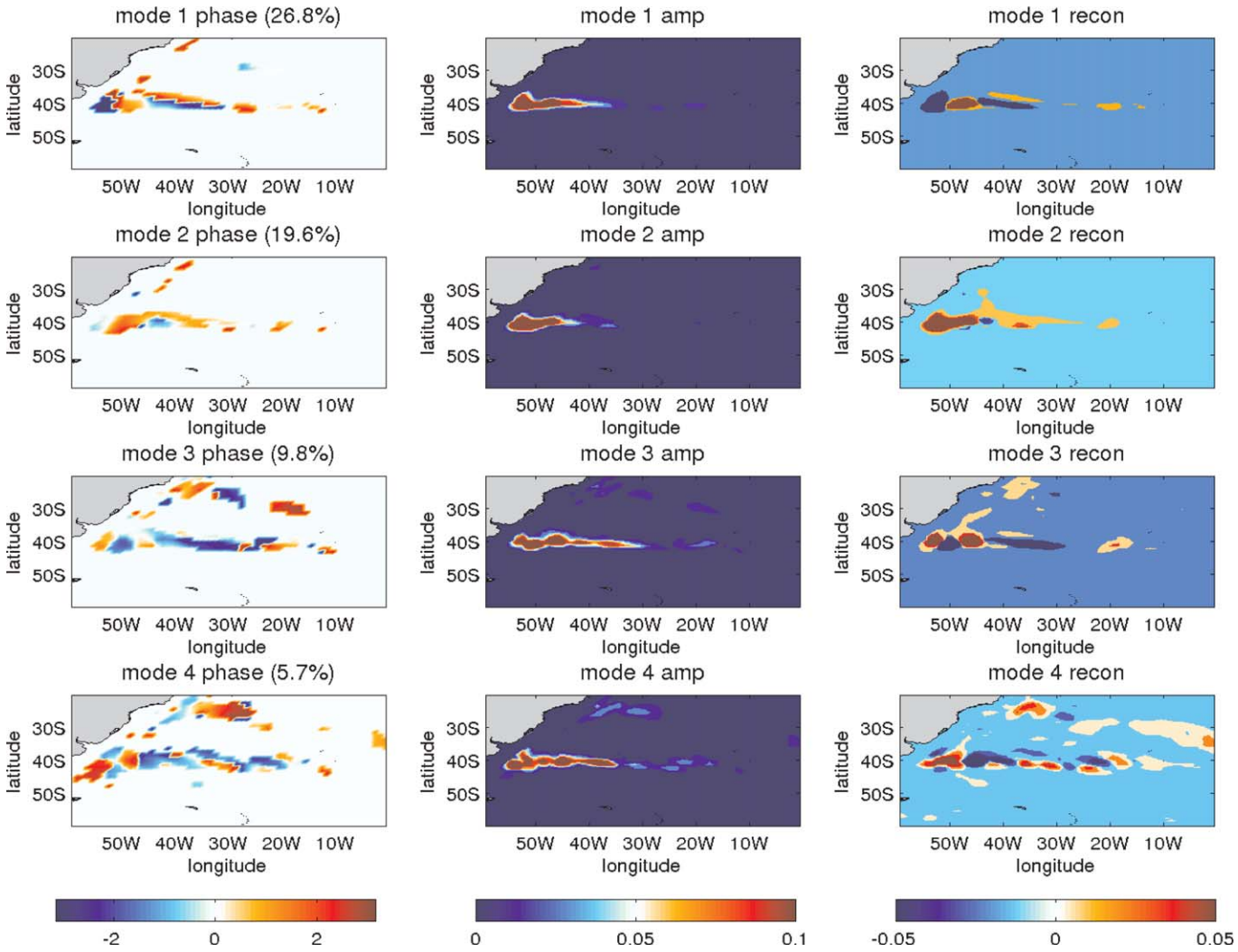

Figure 8. As for Figure 6 but for the South Atlantic. The corresponding temporal amplitudes, phase, and phase portraits are shown in supporting information Figures S5 and S6.

4.2.3. South Pacific Ocean

We now focus with greater detail on the South Pacific. Broadly in agreement with *Maharaj et al.* [2005], the regions where standard deviations of SSH anomalies (Figure 3c) display largest variability are in the East Australian Current (EAC) and at two locations near 50°S between 220°W–200°W and 180°W–160°W (Figure 5). The EAC forms part of the poleward flowing Western Boundary Current (WBC) system associated with the South Pacific subtropical gyre. It forms near 15°S, and flows poleward along Australia's east coast where it tends to separate near Sugarloaf Point (32.5°S) before flowing southeastward into the Tasman Sea and forming the Tasman Front [*Godfrey et al.*, 1980]. On traversing the Tasman Sea and reaching the northernmost part of New Zealand, the East Auckland (EAuC) and East Cape Currents (ECC) are in turn formed. From here it flows southeastward following the New Zealand coast before forming the Wairarapa Eddy, then eastward following the Chatham Rise and finally entering the ACC near the East Pacific Rise [*Tilburg et al.*, 2001]. The region at 50°S between 180°W and 160°W has been shown in the recent study of *O'Kane et al.* [2013] to be associated with large amplitude baroclinic disturbances which propagate into the ACC where they are both slowed and amplified via interaction with the East Pacific Rise.

A CEOF analysis of baroclinic disturbances in the South Pacific (Figure 10) between 210°W and 80°W reveals the EAC to be the dominant region of eddy variability explaining more than 40% of the variance. The mode 2 amplitude is largest about the region (25°–35°S, 160°W) in the region of the Austral seamount chain. Here the CEOF 1 and 2 phase patterns of the real and imaginary PCs (supporting information Figure S8) have

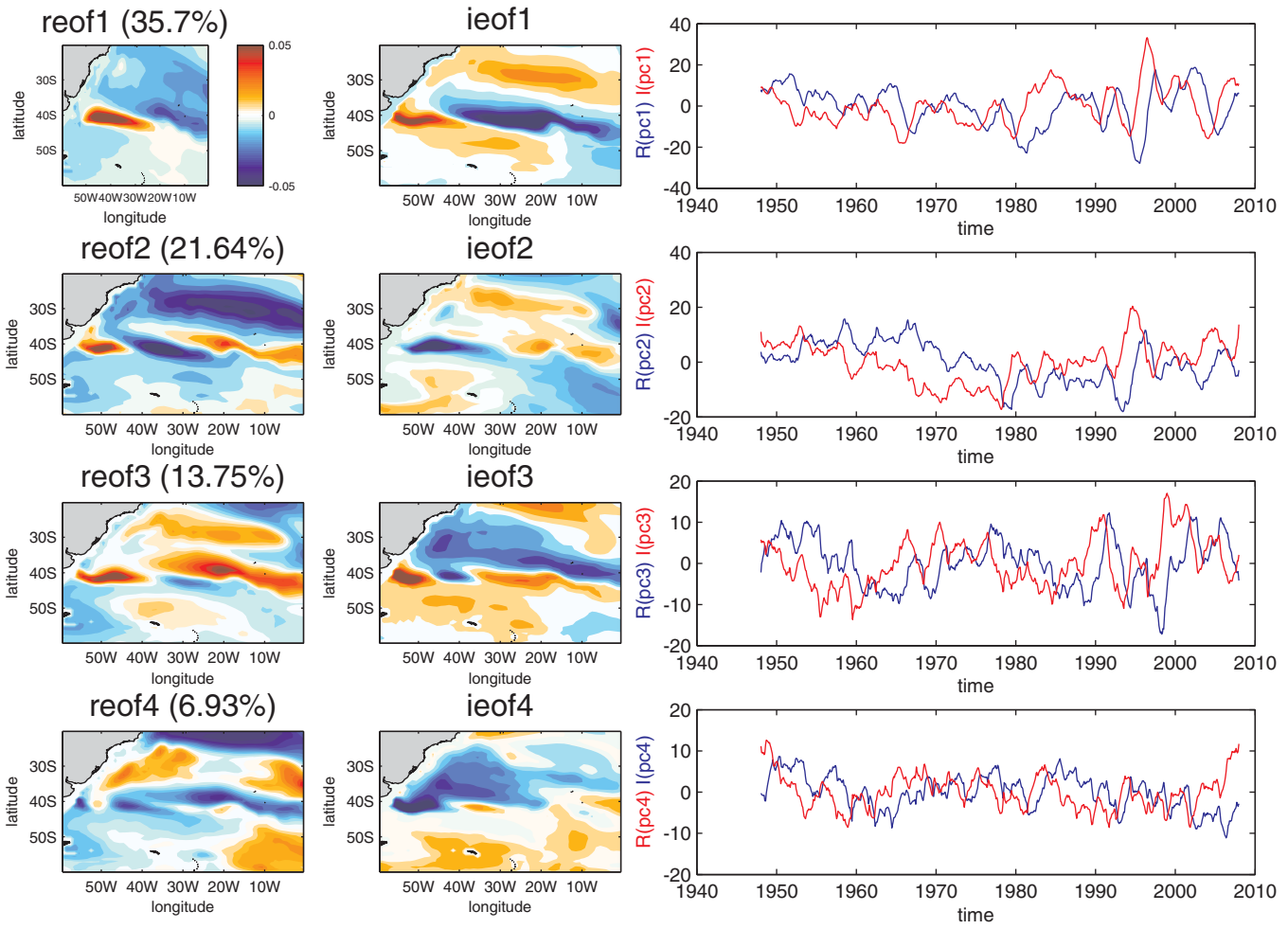

Figure 9. As for Figure 7 but for the South Atlantic. The corresponding temporal amplitudes and phase are shown in supporting information Figure S7.

small phase oscillations and long periods (>10 years) (supporting information Figure S9) and indicating a near stationary pattern. CEOF modes 2–4 explain 11.8%, 8.0%, and 5.1% of the variance, respectively, with phase diagrams of modes 3 and 4 showing that they are the dominant westward propagating modes. As before where the (temporal) phase is decreasing in time (supporting information Figure S9), westward propagation corresponds to continuous decrease in (spatial) phase along the regions of large amplitude (Figure 10, left column). In the Austral seamount region these modes are amplified and a superposition of the leading modes is required to account for a significant amount of the variance. Here it is highly likely that there are processes and strong nonlinearities present such that variances from the leading CEOFs may be potentially spread across many higher-order modes. In the analysis to follow, we apply 2-D-RT methods to identify the dominant propagating modes and their time scales.

In Figure 11, monthly mean baroclinic disturbances Φ' are shown at 2 monthly intervals for the year 2002. These disturbances propagate across the Pacific along mean horizontal density contours where the gradients are large forming a waveguide. The largest amplitudes are coincident with the largest buoyancy frequency anomalies shown in Figure 3b and are also the locations associated with significant bathymetry, i.e., near the Chile Rise 90°W38°S, the East Pacific Rise 35°S110°W and the Austral seamount chain 150°W30°S which lies to the south of the Tuamotu Ridge. These disturbances then propagate westward and though decaying they remain large and coherent until they encounter the Kermadec Ridge (North of New Zealand (38°S) along 180°W) where, consistent with the study of *Moore and Wilkin* [1998], a form of filtering takes place such that disturbances along the Australian shelf are more coherent and regular.

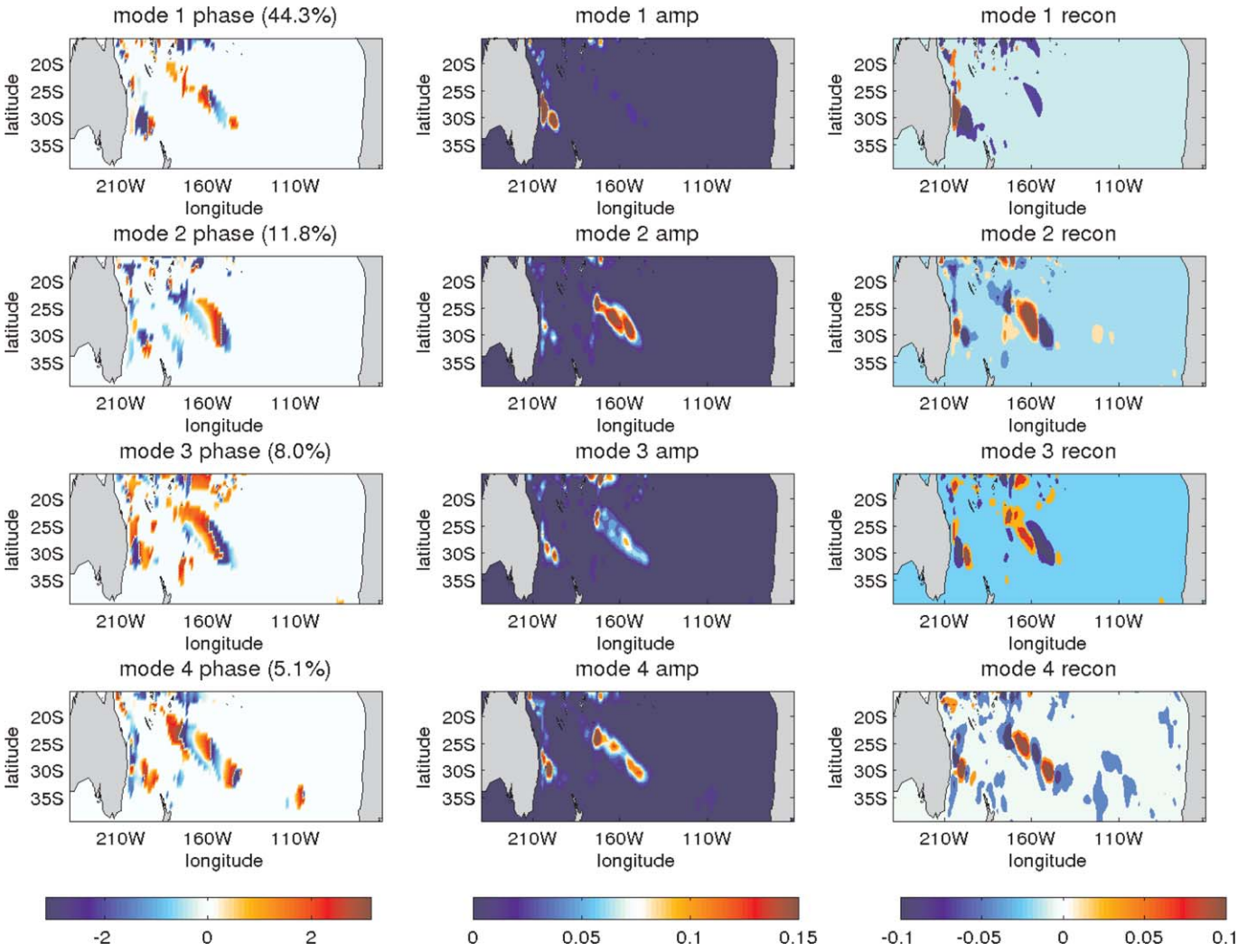

Figure 10. As for Figure 6 but for the South Pacific. The corresponding temporal amplitudes, phase, and phase portraits are shown in supporting information Figures S8 and S9.

Having crossed the Pacific, these disturbances enter the EAC, either directly or via the South Equatorial Current, where they again amplify to form a large-scale coherent wave train [*O'Kane et al*., 2011a]. Some disturbances are subsequently advected via the East Auckland Current into the ACC where they encounter the East Pacific Rise (58°S–60°S, 150°W–155°W) again undergoing amplification via resonance with westward propagating Rossby waves that are swept eastward by the strong mean flow [*Hughes*, 1995]. The propagation and amplification of such disturbances in the ACC was the subject of detailed examination by *O'Kane et al*. [2013].

One question concerning the propagation of baroclinic anomalies across the South Pacific is the speed of propagation. Many studies have proposed that the large-scale wave-like disturbances observed in altimetry broadly obey many of the characteristic behaviors of westward propagating first baroclinic-mode Rossby waves interacting with topography. To investigate this proposition, we now compare the propagation of the unstable baroclinic disturbances with planetary Rossby waves calculated using the shallow water model configuration described earlier (see section 3.2). In Figure 12, gradients of the mean interface depth of the SWM after 30 years integration are shown to be broadly consistent with those of ACCESS-o.

A Hovmoller diagram of interface depth (equivalent to a negative scaling of the surface height) anomalies along the path of best fit to the South Pacific waveguide (Figure 13, left) shows westward linear Rossby wave propagation across the Pacific. For comparison, baroclinic disturbances (at 200 m) from ACCESS-o are averaged along 5° of latitude at each point on the same path (Figure 13, right). Here a 9 month digital filter

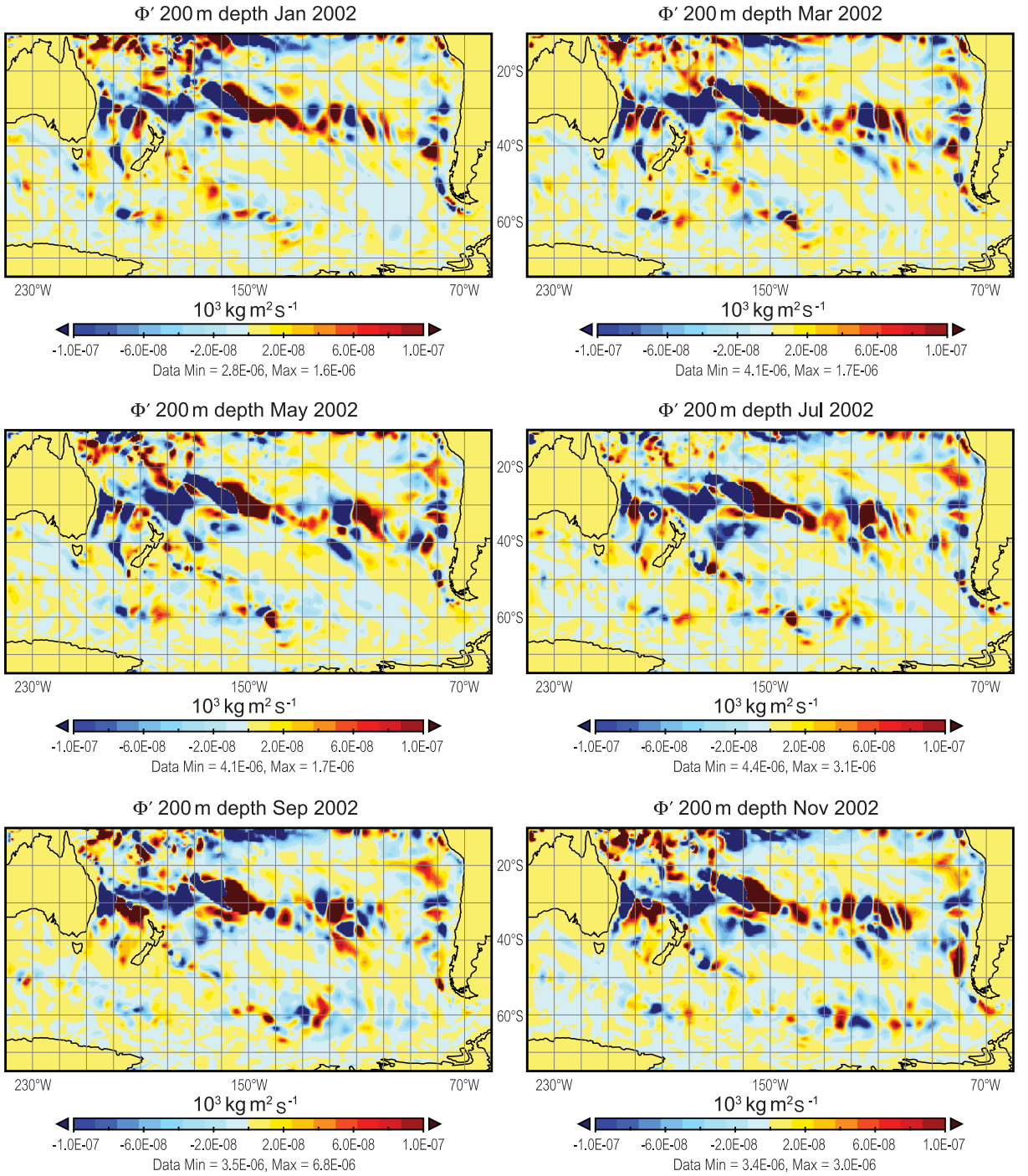

Figure 11. Monthly mean Φ'_{200m} at bimonthly intervals during 2002.

has been applied as well as time centering and standardization such that the scaling is the same. While there are at times similarities between the propagation characteristics of the linear Rossby waves and baroclinic disturbances, in general the propagation of the baroclinic anomalies appears more complex than the linear Rossby waves. This complexity, we will show later, arises from their multiscale nature. For the period 1948–1957 and longitudes between 160°W and the Chilean coast, we see some similarity in the propagation speeds of the respective positive and negative SSH and Φ' anomalies. The period mid 1985–1992 are dissimilar. For latitudes west of about 150°W, the amplitude of the baroclinic disturbances increases. More specifically, we clearly see the amplification (resonance) locations of the Austral seamount chain at 150°W

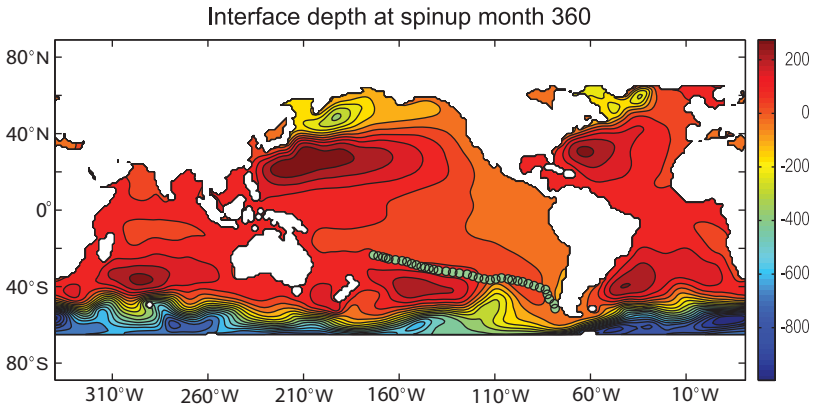

Figure 12. SWM model interface depth (m) after a 30 year spin-up. Circles indicate track for Hovmoller diagram in Figure 13. The total distance is 9925 km.

and the EPR and Chile Rise 100°W–80°W. In the region west of 150°W, we can identify the significant El Niño years: 1953, 1958, 1973, 1983, 1986–1987, 1997–1998, 2003, and 2007.

A 2-D-RT analysis (Figure 14) of the SWM identified a single peak corresponding to a phase speed for planetary Rossby waves of 3.6cms^{-1}. A similar analysis of the Φ' Hovmoller diagram revealed three distinct peaks based on the standard deviation of the transform for any given projection path. The first, at $\approx 6°$, is not a propagating signal but corresponds to resonant amplification of the baroclinically unstable waves with topography. Inverse 2-D-RT (back projection) reveals that this mode is a topographically trapped disturbance (Figure 14; Peak 1) located near the Austral seamount chain. The next broad peak between 42° and 75° corresponds to the slow propagation of the dominant baroclinically unstable modes. These features, where several positive baroclinic anomalies appear to be coincident, persist for long periods and are amplified through resonant interaction with topography. For example, at month 500 (Figure 14; Peak 2), a strong resonant interaction occurs with the Chile Rise. The last peak, centered around 82° reflects the fine-scale

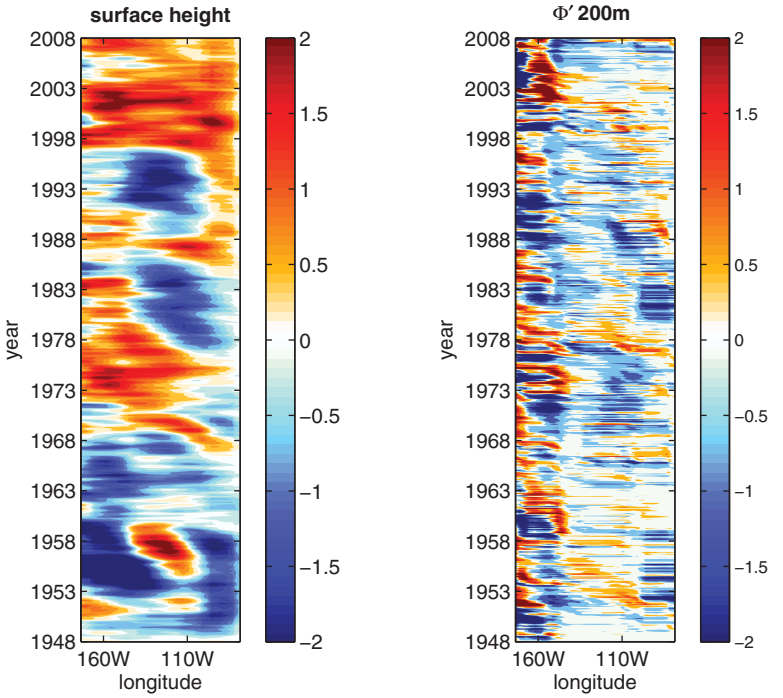

Figure 13. Hovmoller diagrams in time and °W of longitude for (left) SSH (interface depth) from the SWM and (right) Φ' from ACCESS-o. Here Φ' is averaged along 5° of latitude. In both cases, a 9 month digital filter has been applied then time centered and standardized w.r.t., the standard deviation of the full time series.

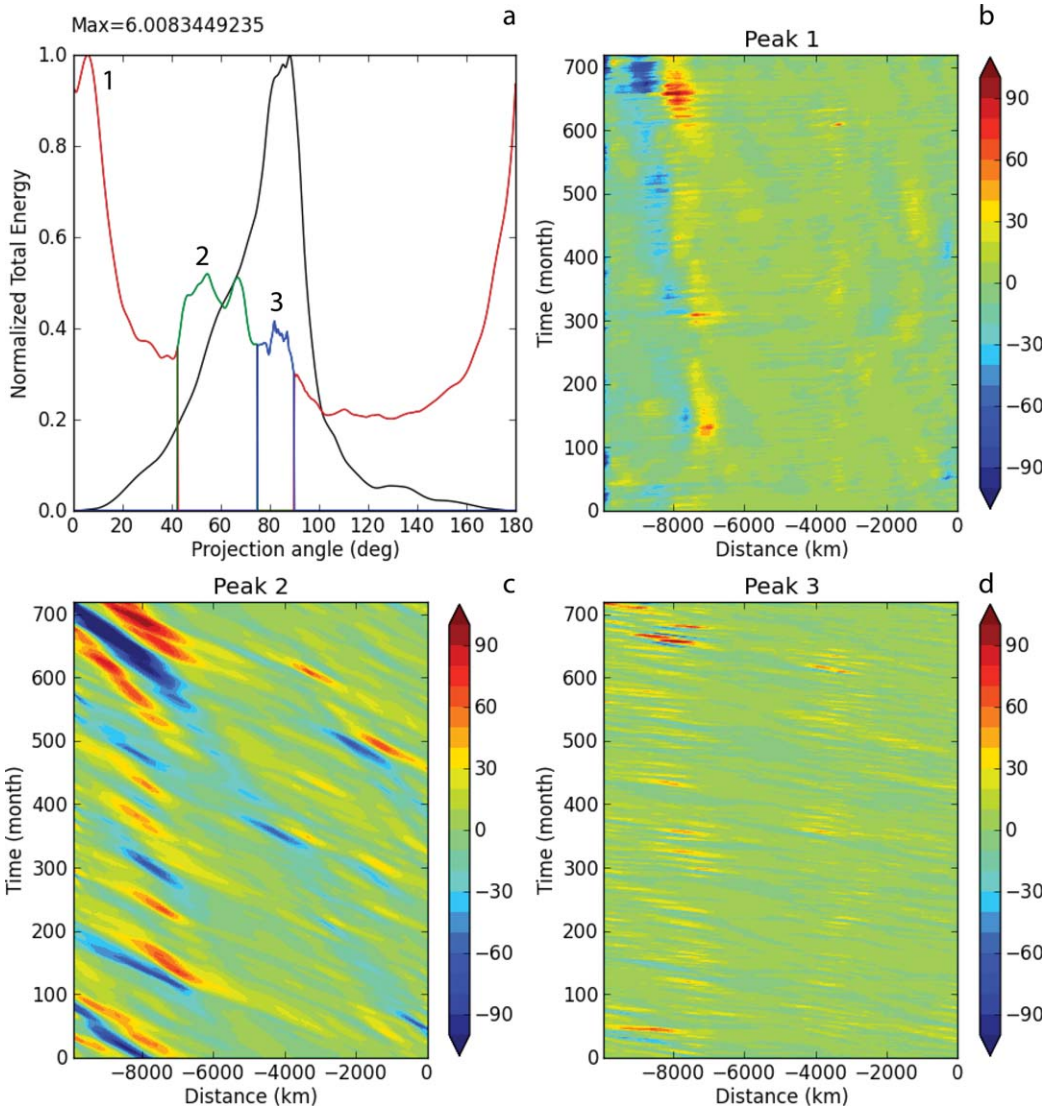

Figure 14. (a) The 2-D-RT analysis of the Φ' Hovmoller diagram (Figure 13, right) identifies three energy peaks whose corresponding back projections reconstruct Hovmoller diagrams of the component modes. Peak 1 (red line) corresponds to a near stationary topographically trapped mode (back projection is shown in plot b). The green line in Figure 14a identifies the dominant unstable baroclinic modes (Peak 2—plot c) propagating at speeds $\approx 1-2\text{cms}^{-1}$. The blue line in Figure 14a identifies weak unstable baroclinic modes (Peak 3—plot d) propagating at speeds of $\approx 3-4\text{cms}^{-1}$ in common with the planetary Rossby wave speed (black line Figure 14 a) calculated from a similar analysis of the SWM interface depth (Figure 13, left). In Figures Figure 14b–14d, distance is kilometers from East to West along the track identified in Figure 12 and the units have been standardized to fall within the range [−100:100] as indicated by the color bars.

propagation of weak Φ' disturbances (Figure 14; Peak 3) propagating at the speed of the planetary Rossby waves (3–4 cm s^{-1}). An inverse 2-D-RT shows these features are more coherent across the basin with interactions with the EPR (≈ -3800km) and the Austral seamount chain (≈ -8000 km). For the 3 peaks (two slow and one fast fine scale), the corresponding phase speeds are 0.74, 1.2, and 3.67 cm s^{-1}, respectively, where the along track distance is 9925 km. The propagation speed of the fine-scale disturbances are comparable but slightly slower than the planetary Rossby wave speeds estimated by *Hill et al*. [2000].

5. Discussion

Maharaj et al. [2005] identified westward propagating South Pacific Rossby waves when considering the energy variability from a 2-D-RT analysis of more than a decade of altimeter data from TOPEX/Poseidon and ERS. They found evidence that long baroclinic Rossby waves interact with isolated bathymetric features such as seamounts at various locations across the South Pacific basin resulting in anomalously slow Rossby

wave phase speeds. Further, *Maharaj et al*. [2007] showed that there is no first baroclinic mode present at the Chile Rise 90°W38°S but that Rossby wave speed estimates in such locations can only be roughly approximated by the extended linear theory baroclinic modes 2 and 3 of *Killworth and Blundell* [2005] (see also *Tailleux* [2012] for a correction to the theory of Killworth and Blundell). In our Figure 14d (Peak 3), we show no significant interactions at the Chile Rise (1800 km) for disturbances traveling at planetary wave speeds but clear resonant interactions, in particular at month 500, for the slower baroclinically unstable waves (Figure 14c; Peak 2) in this region. Our results are consistent with earlier studies [*Killworth and Blundell*, 2005; *Maharaj et al*., 2007] showing that both the linear and extended Rossby wave theories fail to represent the observed energy spectra in the subtropical South Pacific Ocean at 24°S, 160°W and more generally in the western South Pacific between 20°S and 30°S, postulating that this was due to strong nonlinear dynamics arising from high eddy variability. In general, where strong nonlinearities are present, differentiating eddies from waves becomes difficult and both classical and extended linear Rossby wave theory breaks down.

Our results show that westward propagation of large wave-like baroclinic disturbances characterized by Φ' occur on the subtropical fronts in the South Pacific at about 30°S and that the dominant disturbances recovered from a 2-D-RT analysis are large (>300km) multiscale features with three distinct phase speeds; one at planetary Rossby wave speeds, one significantly slower, and one that is topographically trapped. The significant size and slow propagation speeds of these disturbances necessarily implies that they are nonlinearly modified and exist in the eddy saturated wave number range. That is, their growth will necessarily be slower than otherwise predicted assuming linear disturbance growth (exponential separation of initially close trajectories [see *O'Kane et al*., 2011a, and references therein]) such as assumed by *Gill et al*. [1974].

We have shown that in the South Pacific between 24°S and 30°S low-frequency baroclinic disturbances propagate westward in a waveguide determined by horizontal density gradients and amplify in regions where significant topographic features are found. A 2-D-RT analysis has further shown that these nonlinear baroclinically unstable waves may become trapped through resonant interaction where large horizontal density gradients occur coincident with significant isolated topographic structure. Consistent with the linearized theory of *Gill et al*. [1974] there is evidence that some disturbances propagate at the speed of the first baroclinic mode; however, these modes are subdominant and most of the energy of the propagating modes are at the slower speeds as observed by altimetry.

Holbrook et al. [2011] demonstrated the relationship between observed estimates of EAC transport variations calculated from repeat XBT transect data [*Ridgway et al*., 2008] and sea-level observations from the long Fort Denison tide-gauge record in Sydney Harbor. Using a similar configuration of the reduced-gravity shallow water model as used in the present study, they further showed that the El Niño-Southern Oscillation to decadal time scale variations and the multidecadal trend in observed sea level at Fort Denison are significantly correlated with the model simulated modulations in EAC transports by incoming westward propagating (linear baroclinic) oceanic Rossby waves forced by NCEP reanalysis wind stresses over 45 years. Over the period 1970–2003, *Sasaki et al*. [2008] found remotely forced Rossby waves account for the largest contributions to sea-level variances in the Tasman Sea and Tasman Front. Although primarily concerned with deep water processes, *Moore and Wilkin* [1998] suggested that scattering of planetary waves as they pass over the Kermadec ridge was unlikely to be the source of EAC variability. Our Figure 11 shows coherent and regular wave-like features in the EAC as well as some evidence of scattering by the Kermadec Ridge but that the baroclinically unstable waves do propagate through to form coherent wave features in the EAC. In contrast to these earlier studies, we have calculated slow westward propagating disturbances as baroclinically unstable waves and not planetary waves.

Baroclinic disturbances can propagate from the southwest Western Australian coast via one of two pathways to the central south Indian Ocean and a second pathway that connects the Western Australian coast to Madagascar. These results agree with those of *Palastanga et al*. [2007] that local baroclinic instabilities are the source of Rossby wave variability in the subtropical Indian Ocean and the origin of the eddy variability around 25°S. *Palastanga et al*. [2007] used a linear two-layer quasi-geostrophic model without friction or bottom topography to calculate the Phillips criterion and analyze combined hydrographic and altimetric data in the South Indian Ocean over the period 1992–2004. They estimate the unstable frequencies corresponding to periods of 3.5–6 years and wavelengths of about 290–470 km between 24°S and 31°S with the largest growth rates (*e*-folding time scales of $\approx$ 80 days) occurring near 280°W in the region corresponding

to the lower branch we describe here. We find considerable variability evident in the propagation of the Φ' disturbances across the Indian Ocean with particular branches dominating at particular times. For example, the upper branch propagates along the western Australian coast to about Exmouth (21.85°S, ≈ 246°W) before separating to cross the Indian Ocean toward the Seychelles. This branch is dominant at 300 m throughout 1974 and near the end of 1998, for example. The lower branch separates from the coast near Geraldton (28.46°S, ≈ 246°W) traversing the Indian Ocean toward Mauritius. This branch is also evident in 1974 at 300 m and is dominant at 200 m from 2002 through 2006 (not shown).

Having established pathways, subsequent work focusing on the Indian Ocean is required to determine whether our results are consistent with those of *Schouten et al*. [2002] who suggested that the arrival of Rossby waves at 12°S and 27°S modulates eddy variability around Madagascar with a dominant subannual frequency of 4–5 times per year. *Trenary and Han* [2013] revealed decadal variability in terms of vertical displacements of the tropical southwestern Indian Ocean thermocline, between 5°S and 17°S and at a depth of about 200 m, examining the respective roles of changes in wind stress curl and the trade winds. They further examined the role of the internal ocean dynamics on decadal thermocline variability in the region between 20°S and 30°S. Such vertical displacements of the thermocline may indicate the internal stability of the waveguide. As we have already discussed, there is a strong relationship between the amplitude of Φ' and sea surface height. In Figure 3c, we can see a large positive height anomaly in the central Indian Ocean. Significant height anomalies in this region often occur coincident with the arrival of large amplitude disturbances that have propagated along the upper Φ' branch extending to the southwestern coast of Australia (Figures 4a and 6).

The other main regions of large baroclinic disturbances are the tropics and the ACC and, although not the focus of this study, we will mention them briefly for completeness. *O'Kane et al*. [2013] showed that eastward propagation of baroclinically unstable waves occurs along the edge of the Sub-Antarctic Front and within the ACC (Pacific) where Rossby wave propagation is known to be eastward and nonlinear. They showed that amplification occurs primarily through interactions with topography and that the largest amplification occurs coincident with topographic slowing (trapping) of Rossby waves and stochastic forcing due to synoptic weather. They describe in detail the respective roles of baroclinic and barotropic instability in the formation and life time of large-scale wave-like disturbances in the Pacific sector of the ACC.

In the tropical Pacific the major amplification of disturbances occurs due to ENSO and in the region near 5° N is consistent with the instability study of *Hoffman et al*. [2009]. El Niño events generated by Rossby-Kelvin wave resonant interactions cause large influxes of anomalously warm water to the Indian Ocean which are coincident with large baroclinic instabilities. *Ogata and Masumoto* [2010] discuss the link between disturbances propagating from the equatorial Pacific into the Indian Ocean and the Indian Ocean Dipole events of 1994 and 1997–1998 [see also *Wijffels and Meyers*, 2004]. ENSO is very evident in Φ' in the tropics where major El Niño events can be shown to push large disturbances into the Indian Ocean via the Indonesian Throughflow. In the tropics, the significant El Niño events of 1972–1973, 1982–1983, 1997–1998, and 2006–2007 and the changing character of the Central Pacific ENSO or Modoki events (for example, 1979–1980, 1991, 1992, 2002, and 2004 [*Ashok et al*., 2007]) are also associated with tropical instability waves. It remains to be understood how disturbances from the South East Indian Ocean traversing the upper waveguide to the central Indian Ocean might interact with those entering via the Indonesian throughflow. This is the subject of further study.

6. Conclusions

In the subtropics, low-frequency wave-like baroclinic disturbances are observed in regions characterized by relatively fast Eady growth periods (20–50 days). Much work has tried to establish the cause of the observed subtropical SSH variability from altimetry and planetary waves using linear Rossby wave theory. We have proposed an alternate view that remains consistent with the studies of the Sargasso Sea by *Gill et al*. [1974] and *Halliwell et al*. [1994] and the three-dimensional instability theory of *Frederiksen* [1982]. The mechanism by which the disturbances we have described are coherent, propagate along clearly defined pathways and amplify via resonant interaction with topography may be summarized thus:

1. Potential energy of the large-scale mean ocean circulation is generated by the action of the large-scale mean wind field.

2. This energy is converted into eddy energy by baroclinic instability in the regions where subtropical mode water forms.

3. Although these baroclinic disturbances superficially have similar propagation characteristics to planetary Rossby waves they are inherently nonlinear and multiscale and are amplified through resonant interaction with topography.

4. The large spatial scales and wave-like structures suggests eddy energy is projected onto the large scales via the inverse energy cascade according to quasi-geostrophic turbulence theory, much like the way coherent structures form in the atmosphere.

5. These structures are associated with quasi-equilibrium states that develop after the eddy wave number spectrum becomes saturated and long-wavelength coherent structures form. That they are strongly nonlinear and inherently multiscale makes distinguishing them from linear Rossby waves in observations, such as altimetry, an exceedingly difficult task.

More generally, the mechanisms described here offer a further interesting analogue to the midlatitude storm tracks of the atmosphere and oceans. Importantly, they provide a mechanism to communicate information on longer time scales from the midlatitude into the tropical oceans. In order for the baroclinic disturbances we have described to reach the spatiotemporal scales observed by altimetry requires them to have undergone an extended period of nonlinear modification which can only occur as eddy energy saturates [*O'Kane et al*., 2011b]. This is a significant departure from what commonly occurs in atmospheric phenomena such as midlatitude blocking [*O'Kane and Frederiksen*, 2008] whereby disturbances typically have an extended period of linear growth and a relatively short range of scales where eddy saturation can occur. Thus, the wave-like structures we have considered are inherently and strongly nonlinear and require, in order for their growth and decay rates to be calculated accurately, characterization using fundamentally nonlinear dynamical vectors (for example, bred vectors *O'Kane and Frederiksen* [2008], *Hoffman et al*. [2009], and *O'Kane et al*. [2011a]). The application of such nonlinearly modified vectors to characterize disturbance growth is the subject of our current research. It is our hope that such an approach may provide suitable choices to initialize ensemble prediction schemes for decadal prediction in a coupled ocean-atmosphere-ice framework such that we can understand how these disturbances influence atmospheric phenomena.

Acknowledgments
This work was possible thanks to financial support provided by Australian Climate Change Science Program and CSIRO's Wealth from Oceans flagship. T.J.O. is supported by an Australian Research Council (ARC) Future Fellowship. N.J.H. and E.C.J.O. are investigators within the ARC Centre of Excellence for Climate System Science. The authors greatly appreciate the assistance of Louise Bell in preparing the figures for publication.

References

Antonov, J. I., D. Seidov, T. P. Boyer, R. A. Locarnini, A. V. Mishonov, H. E. Garcia, O. K. Baranova, M. M. Zweng, and D. R. Johnson (2010), *World Ocean Atlas 2009, vol. 2, Salinity, NOAA Atlas NESDIS 68*, edited by S. Levitus, pp. 184, U.S. Gov. Print. Off., Washington, D. C.

Ashok, K., S. Behera, S. Rao, H. Weng, and T. Yamagata (2007), El Nino Modoki and its possible teleconnection, *J. Geophys. Res.*, *112*, C11007, doi:10.1029/2006JC003798.

Bonjean, F., and G. Lagerloef (2002), Diagnostic model and analysis of the surface currents in the tropical pacific ocean, *J. Phys. Oceanogr.*, *32*, 2938–2954.

Bretherton, F., and D. Haidvogel (1976), Two-dimensional turbulence above topography, *J. Fluid Mech.*, *78*, 129–154.

Cerovecki, I., and R. A. de Szoeke (2007), How purely wind-driven long planetary geostrophic waves may be energised in the western part of ocean subtropical gyres, *J. Phys. Oceanogr.*, *37*, 60–70.

Challenor, P., P. Cipollini, D. Cromwell, K. Hill, G. Quartly, and I. Robinson (2004), Characteristics of mid-latitude Rossby wave propagation from multiple satellite datasets, *Int. J. Remote Sens.*, *25*, 1297–1302.

Charney, J. (1947), The dynamics of long waves in a baroclinic westerly current, *J. Meteorol.*, *4*, 132–162.

Chelton, D., and M. G. Schlax (1996), Global observations of oceanic Rossby waves, *Science*, *272*, 234–238.

Chelton, D., R. de Szoeke, and M. Schlax (1998), Geographical variability of the first baroclinic Rossby radius of deformation, *J. Phys. Oceanogr.*, *28*, 433–460.

Chelton, D., M. G. Schlax, and R. Samelson (2011), Global observations of nonlinear mesoscale eddies, *Prog. Oceanogr.*, *91*, 167–216.

Chen, C., and I. Kamenkovich (2013), Effects of topography on baroclinic instability, *J. Phys. Oceanogr.*, *43*, 790–804.

de Miranda, A., B. Barnier, and W. Dewar (1999), On the dynamics of the Zapiola anticyclone, *J. Geophys. Res.*, *104*, 21,137–21,149.

Delworth, T., A. Broccoli, A. Rosati, R. Stouffer, V. Balaji, J. Beesley, W. Cooke, and K. Dixon (2006), GFDL's CM2 global coupled climate models. Part 1: Formulation and simulation characteristics, *J. Clim.*, *19*, 643–674.

Eady, E. (1949), Long waves and cyclone waves, *Tellus*, *1*, 33–52.

Early, J., R. Samelson, and D. Chelton (2011), The evolution and propagation of quasigeostrophic ocean eddies, *J. Phys. Oceanogr.*, *41*, 1535–1555.

Frederiksen, J. (1982), A unified three–dimensional instability theory on the onset of blocking and cyclogenesis, *J. Atmos. Sci.*, *39*, 969–982.

Frederiksen, J., and T. J. O'Kane (2005), Inhomogeneous closure and statistical mechanics for Rossby wave turbulence over topography, *J. Fluid Mech.*, *539*, 137–165.

Freeman, T. G. (2010), *The mathematics of Medical Imaging, Springer Undergraduate Texts in Mathematics and Technology*, Springer Science and Business Media, LLC, Springer, N. Y., doi:10.1007/978-0-387-92712-1_2.

Fu, L., and D. B. Chelton (2001), Large scale ocean circulation, in *Satellite Alitmetry and Earth Sciences*, pp. 133–169, Elsevier, N. Y.

Gill, A., J. Green, and A. Simmons (1974), Energy partition in the large-scale ocean circulation and the production of mid-ocean eddies, *Deep Sea Res. Oceanogr. Abstr.*, *21*, 499–528.

Gill, A. E. (1982), *Atmosphere-Ocean Dynamics*, Elsevier, N. Y.
Godfrey, J., G. Cresswell, T. Golding, A. Pearce, and R. Boyd (1980), The separation of the east australian current, *J. Phys. Oceanogr.*, *10*, 430–440.
Gray, A. R., and S. C. Riser (2014), A global analysis of Sverdrup balance using absolute geostrophic velocities from Argo, *J. Phys. Oceanogr.*, *44*, 1213–1229.
Green, J. (1974), Transfer properties of the large-scale eddies and the general circulation of the atmosphere, *Q. J. R. Meteorol. Soc.*, *96*, 157–185.
Griffies, S., et al. (2009), Coordinated Ocean-ice Reference Experiments (COREs), *Ocean Modell.*, *26*, 1–46.
Haidvogel, D., and A. Beckmann (1999), *Numerical Ocean Circulation Modeling*, 320 pp., Imp. Coll. Press, London, U. K.
Halliwell, G., G. Peng, and D. Olson (1994), Stability of the Sargasso sea subtropical frontal zone, *J. Phys. Oceanogr.*, *24*, 1166–1183.
Hannachi, A., I. Jolliffe, and D. Stephenson (2007), Empirical orthogonal functions and related techniques in atmospheric science: A review, *Int. J. Climatol.*, *27*, 1119–1152.
Hill, K., I. Robinson, and P. Cipollini (2000), Propagation characteristics of extratropical planetary waves observed in the ATSR global sea surface temperature record, *J. Geophys. Res.*, *105*, 21,927–21,945.
Hoffman, M., E. Kalnay, J. Carton, and S.-C. Yang (2009), Use of breeding to detect and explain instabilities in the global ocean, *Geophys. Res. Lett.*, *36*, L12608, doi:10.1029/2009GL037729.
Holbrook, N., and A. Maharaj (2008), Southwest pacific subtropical mode water: A climatology, *Prog. Oceanogr.*, *77*, 298–315.
Holbrook, N., I. Goodwin, S. McGregor, E. Molina, and S. Power (2011), ENSO to multi-decadal time scale changes in East Australian Current transports and Fort Denison sea level: Oceanic Rossby waves as the connecting mechanism, *Deep Sea Res., Part II*, *58*, 547–558.
Hughes, C. (1995), Rossby waves in the southern ocean: A comparison of TOPEX/POSEIDON altimetry with model predictions, *J. Geophys. Res.*, *100*, 15,933–15,950.
Kessler, W. (1990), Observations of long Rossby waves in the northern tropical Pacific, *J. Geophys. Res.*, *95*, 5183–5217.
Killworth, P., and J. Blundell (1999), The effect of bottom topography on the speed of long extratropical planetary waves, *J. Phys. Oceanogr.*, *29*, 2689–2710.
Killworth, P., and J. Blundell (2005), The dispersion relation for planetary waves in the presence of mean flow and topography. Part II: Two-dimensional examples and global results, *J. Phys. Oceanogr.*, *35*, 2110–2133.
Large, W., and S. Yeager (2004), Diurnal to decadal global forcing for ocean and sea-ice models: The datasets and flux climatologies, *NCAR Tech. Note NCAR/TN-460+STR*, CGD Div. of the Natl. Cent. for Atmos. Res.
Large, W., and S. Yeager (2009), The global climatology of an interannually varying air-sea flux data set, *Clim. Dyn.*, *33*, 341–364.
Large, W., J. McWilliams, and S. Doney (1994), Oceanic vertical mixing: A review and a model with a nonlocal boundary layer parameterization, *Rev. Geophys.*, *32*, 363–403.
Locarnini, R. A., A. V. Mishonov, J. I. Antonov, T. P. Boyer, H. E. Garcia, O. K. Baranova, M. M. Zweng, and D. R. Johnson (2010), *World Ocean Atlas 2009, vol. 1, Temperature, NOAA Atlas NESDIS 68*, edited by S. Levitus, pp. 184, U.S. Gov. Print. Off., Washington, D. C.
Maharaj, A., P. Cipollini, and N. Holbrook (2005), Observed variability of the South Pacific westward sea level anomaly signal in the presence of bottom topography, *Geophys. Res. Lett.*, *32*, L04611, doi:10.1029/2004GL020966.
Maharaj, A., P. Cipollini, N. Holbrook, P. Killworth, and J. Blundell (2007), An evaluation of the classical and extended Rossby wave theories in explaining spectral estimates of the first few baroclinic modes in the South Pacific Ocean, *Ocean Dyn.*, *57*(3), 173–187, doi:10.1007/s10236-006-0099-5.
Maharaj, A., P. Cipollini, and N. Holbrook (2009), Multiple westward propgating signals in South Pacific sea level anomalies, *J. Geophys. Res.*, *114*, C12016, doi:10.1029/2008JC004799.
Mata, M., S. Wijffels, J. Church, and M. Tomczak (2006), Eddy shedding and energy conversions in the East Australian Current, *J. Geophys. Res.*, *111*, C09034, doi:10.1029/2006JC003592.
McDougall, T., and P. McIntosh (1996), The temporal-residual-mean velocity. Part I: Derivation and the scalar conservation equations, *J. Phys. Oceanogr.*, *26*, 2653–2665.
Merrifield, M., and R. Guza (1990), Detecting propagating signals with complex empirical orthogonal functions: A cautionary note, *J. Phys. Oceanogr.*, *20*, 1628–1633.
Moore, M., and J. Wilkin (1998), Variability in the south Pacific deep western boundary current from current meter observations and a high resolution global model, *J. Geophys. Res.*, *103*, 5439–5457.
Murray, R. (1996), Explicit generation of orthogonal grids for ocean models, *J. Comput. Phys.*, *126*, 251–273.
Oey, L.-Y. (2008), Loop current and deep eddies, *J. Phys. Oceanogr.*, *38*, 1426–1449.
Ogata, T., and Y. Masumoto (2010), Interactions between mesoscale eddy variability and Indian Ocean dipole events in the Southeastern tropical Indian Ocean—Case studies for 1994 and 1997/1998, *Ocean Dyn.*, *60*, 717–730.
O'Kane, T., and J. Frederiksen (2004), The qdia and regularized qdia closures for inhomogeneous turbulence above topography, *J. Fluid Mech.*, *504*, 133–165.
O'Kane, T., and J. Frederiksen (2008), A comparison of statistical dynamical and ensemble prediction methods during blocking, *J. Atmos. Sci.*, *65*, 426–447.
O'Kane, T., P. Oke, and P. Sandery (2011a), Predicting the East Australian Current, *Ocean Modell.*, *38*, 251–266.
O'Kane, T., P. Oke, and P. Sandery (2011b), Ensemble prediction study of the East Australian Current, *ANZIAM J.*, *52*, C38–C55.
O'Kane, T., R. Matear, M. Chamberlain, J. Risbey, B. Sloyan, and I. Horenko (2013), Decadal variability in an OGCM Southern Ocean: Intrinsic modes, forced modes and metastable states, *Ocean Modell.*, *69*, 1–21.
Orlanski, I., and M. Cox (1973), Baroclinic instability in ocean currents, *Geophys. Fluid Dyn.*, *4*, 297–332.
Palastanga, V., P. J. van Leeuwen, M. W. Schouten, and W. P. M. de Ruijter (2007), Flow structure and variability in the subtropical Indian Ocean: Instability of the South Indian Ocean countercurrent, *J. Geophys. Res.*, *112*, C01001, doi:10.1029/2005JC003395.
Pedlosky, J. (1964), The stability of currents in the atmosphere and in the ocean. Part I, *J. Atmos. Sci.*, *21*, 201–219.
Phillips, N. (1954), Energy transformations and meridional circulations associated with simple baroclinic waves in a two-level, quasigeostrophic model, *Tellus*, *6*, 273–286.
Qiu, B., and S. Chen (2004), Seasonal modulations in the eddy field of the South Pacific Ocean, *J. Phys. Oceanogr.*, *34*, 1515–1527.
Rasmusson, E., P. Arkin, W.-Y. Chen, and J. Jalickee (1981), Biennial variations in surface temperature over the United States as revealed by singular decomposition, *Mon. Weather Rev.*, *109*, 587–598.
Ridgway, K., R. Coleman, R. Bailey, and P. Sutton (2008), Decadal variability of East Australian Current transport inferred from repeated high-density XBT transects, a CTD survey and satellite altimetry, *J. Geophys. Res.*, *113*, C08039, doi:10.1029/2007JC004664.

Sasaki, Y., S. Minobe, N. Schneider, T. Kagimoto, M. Nonaka, and H. Sasaki (2008), Decadal sea level variability in the South Pacific in a global eddy-resolving ocean model hindcast, *J. Phys. Oceanogr.*, *38*, 1731–1747.
Schouten, M., W. P. de Ruijter, and P. J. van Leeuwen (2002), Upstream control of Agulhas Ring shedding, *J. Geophys. Res.*, *107*, C83109, doi: 10.1029/2001JC000804.
Smagorinsky, J. (1963), General circulation experiments with the primitive equations, *Mon. Weather Rev.*, *91*, 99–164.
Smith, K. S. (2007), The geography of linear baroclinic instability in Earths oceans, *J. Mar. Res.*, *65*, 655–683.
Speich, S., B. Blanke, and W. Cai (2007), Atlantic meridional overturning circulation and the Southern Hemisphere supergyre, *Geophys. Res. Lett.*, *34*, L23614, doi:10.1029/2007GL031583.
Tailleux, R. (2003), Comments on the effect of bottom topography on the speed of long extra-tropical Rossby waves, *J. Phys. Oceanogr.*, *33*, 1536–1541.
Tailleux, R. (2005), The quasi-nondispersive regimes of long extratropical baroclinic Rossby waves over (slowly varying) topography, *J. Phys. Oceanogr.*, *36*, 104–121.
Tailleux, R. (2012), On the generalised eigenvalue problem for the Rossby wave vertical velocity in the presence of mean flow and topography, *J. Phys. Oceanogr.*, *42*, 1044–1050.
Tailleux, R., and J. C. McWilliams (2001), The effect of bottom pressure decoupling on the speed of extratropical, baroclinic Rossby waves, *J. Phys. Oceanogr.*, *31*, 1461–1476.
Tailleux, R., and J. C. McWilliams (2002), Energy propagation of long, extratropical Rossby waves over slowly varying zonal topography, *J. Fluid Mech.*, *473*, 295–319.
Talley, L. D. (1999), Some aspects of ocean heat transport by the shallow, intermediate and deep overturning circulations, in *Mechanisms of Global Climate Change at Millenial Time Scales, Geophys. Monogr. Ser.*, vol. 112, edited by P. U. Clark, R. S. Webb, and L. D. Keigwin, pp. 1–22, AGU, Washington, D. C.
Tchernia, P. (1980), *Descriptive Regional Oceanography*, Elsevier, N. Y.
Tilburg, C., H. Hurlburt, J. O'Brien, and J. Shriver (2001), The dynamics of the East Australian Current system: The Tasman Front, the East Auckland Current, and the East Cape Current, *J. Phys. Oceanogr.*, *31*, 2917–2943.
Trenary, L., and W. Han (2013), Local and remote forcing of decadal sea level and thermocline depth variability in the South Indian Ocean, *J. Geophys. Res. Oceans*, *118*, 381–398, doi:10.1029/2012JC008317.
Tulloch, R., J. Marshall, and K. S. Smith (2009), Interpretation of the propagation of surface altimetric observations in terms of planetary Rossby waves and geostrophic turbulence, *J. Geophys. Res.*, *114*, C02005, doi:10.1029/2008JC005055.
Tulloch, R., J. Marshall, and C. Hill (2011), Scales, growth rates, and spectral fluxes of baroclinic instability in the ocean, *J. Phys. Oceanogr.*, *41*, 1057–1076.
Uotilla, P., S. O'Farrell, S. Marsland, and D. Bi (2012), A sea-ice sensitivity study with a global ocean-ice model, *Ocean Modell.*, *51*, 1–18.
Volkov, D., and L. Fu (2008), The role of vorticity fluxes in the dynamics of the Zapiola anticyclone, *J. Geophys. Res.*, *113*, C11015, doi: 10.1029/2008JC004841.
Wang, L., C. Koblinsky, S. Howden, and B. Beckley (1998), Large-scale Rossby wave in the mid-latitude South Pacific from altimetry data, *Geophys. Res. Lett.*, *25*, 179–182.
Wijffels, S., and G. Meyers (2004), An intersection of oceanic waveguides: Variability in the Indonesian Throughflow Region, *J. Phys. Oceanogr.*, *34*, 1232–1253.
Williams, R. G., C. Wilson, and C. W. Hughes (2007), Ocean and atmosphere storm tracks: The role of eddy vorticity forcing, *J. Phys. Oceanogr.*, *37*, 2267–2289.